ELSEVIER

Chemical Geology 243 (2007) 317–343

CHEMICAL GEOLOGY
INCLUDING ISOTOPE GEOSCIENCE

www.elsevier.com/locate/chemgeo

Permian flood basalts and mafic intrusions in the Jinping (SW China)–Song Da (northern Vietnam) district: Mantle sources, crustal contamination and sulfide segregation

Christina Yan Wang *, Mei-Fu Zhou, Liang Qi

Department of Earth Sciences, The University of Hong Kong, Hong Kong, China

Received 7 August 2006; received in revised form 16 May 2007; accepted 20 May 2007

Editor: S.L. Goldstein

Abstract

The ~260-Ma Emeishan large igneous province (ELIP) in SW China and northern Vietnam includes high-Ti and low-Ti volcanic rocks and coeval mafic–ultramafic plutons. In the Jinping (SW China)–Song Da (northern Vietnam) district, the southernmost part of the ELIP, basalts and gabbros of the high-Ti series displays a narrow range of $\varepsilon Nd(t)$ values (+0.5 to +1.1) and low primitive mantle-normalized Th/Nb ratios (~1.4), similar to those of an OIB-like enriched mantle source. The rocks have chondrite-normalized REE patterns enriched in LREE and depleted in HREE. This feature, together with low Al_2O_3/TiO_2 ratios (~4), indicates that the primary melts were generated by small degrees of partial melting at garnet stable depths. The low-Ti series includes LREE-depleted and LREE-enriched picrites, basalts, olivine gabbros and gabbros. The LREE-depleted picrites have chondrite-normalized Ce/Yb ratios of 0.4–0.5, very positive $\varepsilon Nd(t)$ values (+7.0), and very negative Th anomalies in primitive mantle-normalized trace element patterns. They were formed by high degrees of partial melting of a strongly depleted mantle source at relatively shallow mantle depths. The LREE-enriched picrites have very negative $\varepsilon Nd(t)$ values (−7.8) that indicate a mantle source locally modified by subducted oceanic crust. Highly variable chemical compositions and $\varepsilon Nd(t)$ values (+6.4 to −10.2) of the low-Ti basalts and gabbros are attributed to variable degrees of upper crustal contamination of the picritic parental magmas. Therefore, the extrusive and intrusive rocks in this region clearly formed from heterogeneous mantle sources. Crustal contamination triggered S-saturation of some low-Ti magmas and resulted in segregation of immiscible sulfide melts and generation of magmatic Ni–Cu–(PGE) sulfide deposits in this region. Eruption of magmas after sulfide segregation formed PGE-depleted low-Ti basalts.

Keywords: Flood basalts; Mafic intrusions; Geochemistry; SW China; Northern Vietnam; Emeishan large igneous province

1. Introduction

As major constituents of large igneous provinces (LIPs), continental flood basalts are commonly associated with mafic–ultramafic intrusions, some of which may have been the magma chambers and/or the conduits that fed the overlying basalts (Pirajno, 2000). They are commonly interpreted as the products of mantle plumes (Campbell and Griffiths, 1990; White and McKenzie, 1995). Geochemical features of the flood basalts and mafic–ultramafic intrusions have been used to investigate

* Corresponding author. Fax: +852 2517 6912.
E-mail address: wangyan2002@graduate.hku.hk (C.Y. Wang).

0009-2541/$ - see front matter © 2007 Elsevier B.V. All rights reserved.
doi:10.1016/j.chemgeo.2007.05.017

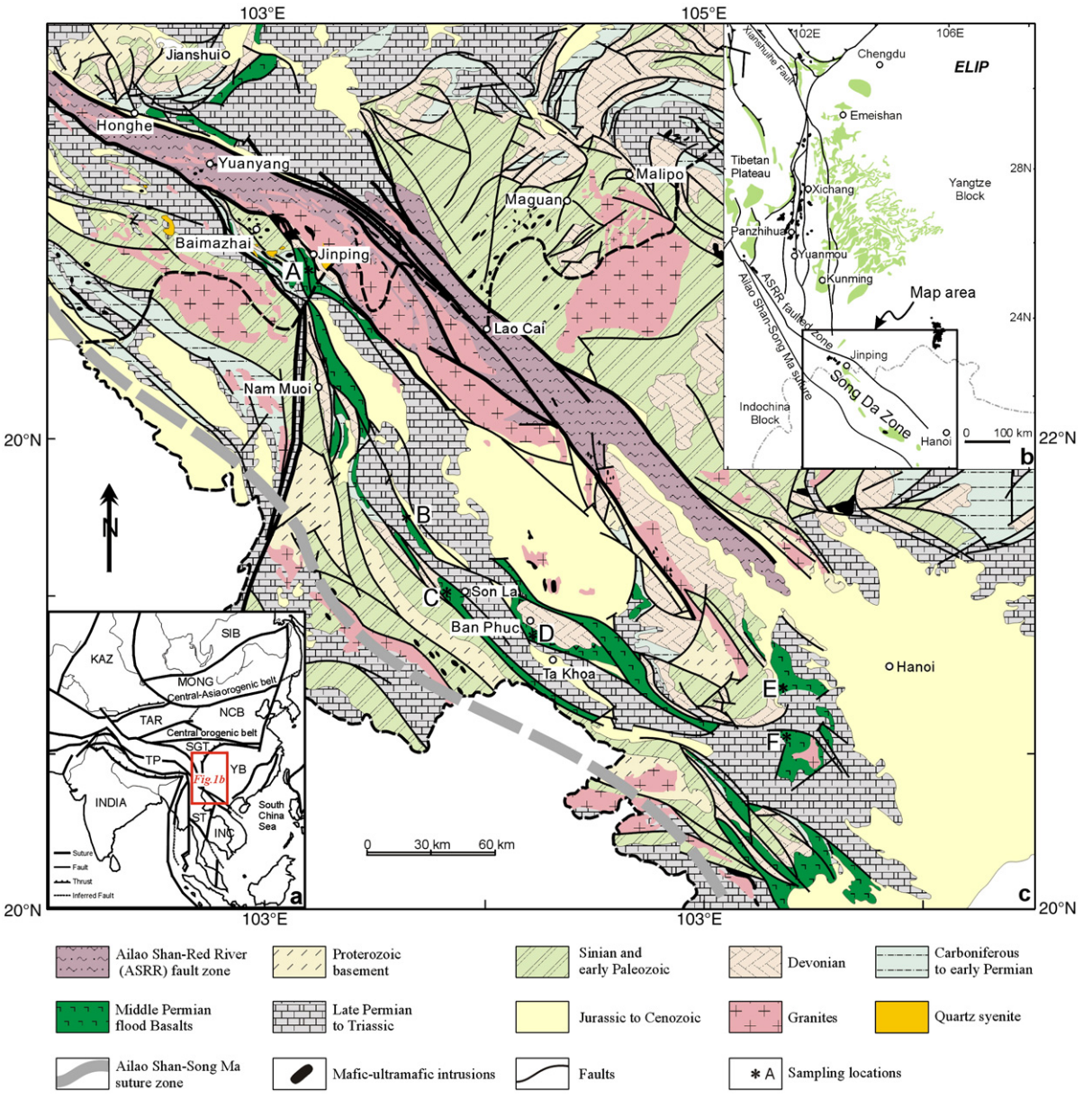

Fig. 1. Geological map of the Emeishan Large Igneous Province in SW China and northern Vietnam showing the distribution of flood basalts and mafic–ultramafic intrusions (after 1:1,000,000 Yunnan Geological Map and Vietnamese Geological Map). The major blocks shown in inset (a) are SIB, Siberia; MONG, Mongolia; NCB, North China Block; YB, Yangtze Block; INC, Indochina Block; TAR, Tarim; KAZ, Kazakhstan; TP, Tibetan Plateau; SGT, Songpan–Ganze terrane; ST, Simao terrane.

the generation and geodynamic setting of LIPs and formation of associated ore deposits (Ernst et al., 2005). It has been documented that there are links between sulfide mineralization hosted in mafic–ultramafic sills and overlying flood basalts in the Noril'sk region of the Siberia Traps (Lightfoot and Keays, 2005), West Greenland (Keays and Lightfoot, 2007), and the Yangliuping area of the Emeishan large igneous province (ELIP) (Song et al., 2006).

The ~260-Ma ELIP in SW China and northern Vietnam includes voluminous continental flood basalts that are believed to have formed from an upwelling mantle plume (Chung and Jahn, 1995; Xu et al., 2001, 2004; Zhou et al., 2006). The role of mantle plumes in

generating such basaltic magmas is not clear, and the involvement of lithospheric mantle and continental crust has not been satisfactorily evaluated (Xu et al., 2001; Song et al., 2001; Xiao et al., 2004). Xu et al. (2001) recognized high-Ti and low-Ti lavas in the ELIP on the basis of TiO_2 contents and Ti/Y ratios of the rocks. They proposed that both varieties originated from a mantle plume, with more extensive crustal contamination in the low-Ti basalts than in the high-Ti basalts. Song et al. (2001) proposed that the original melts derived from the mantle plume were contaminated through interaction at shallow depths with an enriched lithospheric mantle. Xiao et al. (2004) argued that the low-Ti melts formed from an enriched continental lithospheric mantle at relatively shallow depths, whereas the high-Ti magmas formed from a deeper mantle source associated with a plume.

Evolution of basaltic magmas and its relationship with the formation of Ni–Cu–(PGE) sulfide deposits in the ELIP have been addressed for the rocks in the Yangliuping area, northernmost part of the ELIP (Song et al., 2006). The flood basalts and mafic–ultramafic intrusions in the Jinping–Song Da district mark the southernmost part of the ELIP (Wu, 1993; Chung et al., 1997; Xiao et al., 2003). The rocks include high-Ti and low-Ti varieties with variable compositions. Some low-Ti picrites in the Song Da area are particularly useful for characterizing mantle sources because they may have been formed by high degree of partial melting and preserved the trace element ratios of the source area (Campbell, 1998). The diversity of the rocks is thus ideal for examining some fundamental questions regarding the ELIP: (1) mantle sources of the high-Ti and low-Ti parental melts; (2) processes involved in the evolution of these magmas; and (3) genetic relationship, if any, between the flood basalts and mafic–ultramafic intrusions in terms of crustal contamination and sulfide mineralization.

Because platinum-group elements (PGE) partition into sulfides much more readily than into silicates, they can provide very robust constraints on the sulfide saturation history of mafic magmas (Peach et al., 1994). Thus, PGE concentrations, combined with major and trace element and Sr–Nd isotopic data for the flood basalts and mafic intrusions in the Jinping–Song Da district, will provide important constraints on the diversity of rocks and ore formation. This paper presents new geochemical dataset in order to investigate the petrogenesis of the basaltic magmas, from their formation in the mantle to their emplacement at the surface or intrusion into the country rock. We also discuss the associated processes leading to sulfide saturation in the melts and the formation of the Ni–Cu–(PGE) sulfide deposits in the Jinping–Song Da district.

2. Geological background

The ELIP in the western part of the Yangtze Block and the eastern margin of the Tibetan Plateau is bounded to the south by the Indochina Block (inset in Fig. 1). The ELIP is mainly composed of flood basalts and mafic–ultramafic intrusions. The flood basalts crop out chiefly in Yunnan, Sichuan and Guizhou Provinces of China and the Song Da region in the northern Vietnam. The volcanic sequence ranges in thickness from several hundred meters in the east to nearly 5 km in the west (Chung and Jahn, 1995; Song et al., 2001; Xu et al., 2001; Xiao et al., 2004). The lavas include picrites, tholeiites and basaltic andesites, all of which are believed to have formed by melting associated with the Emeishan plume (Chung and Jahn, 1995; Xu et al., 2001).

Permian flood basalts and associated mafic–ultramafic intrusions form a narrow ($\leq$20 km), NW-trending belt more than 350 km long in the Jinping–Song Da district. The belt is bounded by the Ailao Shan–Red River fault zone to the northeast and the Ailao Shan–Song Ma suture to the southwest. The flood basalts that crop out in the belt represent the southernmost part of the ELIP (Chung et al., 1997; Xiao et al., 2003) (Fig. 1). The flood basalts unconformably overlie the early Permian limestones, and are concordantly overlain by the early Triassic limestone and shale with coal measures (YBGMR, 2000; Glotov et al., 2001). Folded Triassic sedimentary rocks are unconformably overlain by Cretaceous conglomerates, sandstones and pelites (Lacassin et al., 1998).

The flood basalts crop out in the Nam Muoi River area (>30 km long and ~3 km wide), the Ta Khoa area (60 km long and 10 km wide) and the Jinping area (~150 km^2). The total thicknesses of the lava pile range from about 1100 to 4600 m (1:200,000 Geological Map of the Socialist Republic of Vietnam, 1978; YBGMR, 2000). The low-Ti volcanic sequence includes volcanic breccias, basaltic tuffs and massive basalt flows (Xiao et al., 2003). Low-Ti picrites occur mainly in the Nam Muoi River area (Polyakov et al., 1991; Hanski et al., 2004). The high-Ti basalts are associated with trachydacite, trachyrhyolite and minor high-Ti picrite and andesite (Polyakov et al., 1991, 1998).

Numerous mafic–ultramafic plutons, including differentiated and undifferentiated bodies, intruded Ordovician and Devonian strata in the Jinping–Song Da district. Near the town of Jinping, more than 100 mafic dykes occur in an area of ~20 km^2. They typically range from tens of centimeters to several hundred meters in width and up to tens of kilometers in length. In the Baimazhai area, there

Table 1
Major and trace elements of the flood basalts in the Jinping–Song Da district

Samples	HK-11	HK-13	HK-14	HK-22	HK-24	HK-35	HK-36	HK-37	HK-38	HK-39	HK-42	HK-43	HK-44	HK-46	HK-52
Sites	F	F	F	B	B	B–C	B–C	B–C	B–C	B–C	B–C	B–C	B–C	B–C	B–C
Rock types	High-Ti basalt														
Major oxides (wt.%)															
SiO_2	48.29	51.62	48.24	51.64	47.94	47.15	46.39	46.84	47.60	46.49	49.30	49.62	46.83	48.10	47.56
TiO_2	2.84	2.88	3.45	3.52	3.54	2.56	2.50	2.72	2.76	2.28	3.88	3.89	4.11	2.55	2.69
Al_2O_3	13.23	11.85	12.10	12.32	13.24	13.43	12.66	13.00	13.00	13.82	12.93	12.86	13.59	13.65	13.31
$Fe_2O_3(t)$	12.74	12.04	13.91	13.41	13.09	12.82	13.71	13.24	12.46	12.19	13.64	13.45	14.19	13.15	13.21
MnO	0.22	0.20	0.23	0.15	0.14	0.23	0.17	0.23	0.25	0.18	0.14	0.13	0.20	0.21	0.23
MgO	4.79	5.02	5.59	3.83	4.50	6.17	5.46	7.04	6.88	6.33	3.54	3.48	4.63	5.95	6.03
CaO	9.11	6.29	7.91	4.80	7.44	7.89	8.05	6.93	6.53	9.34	5.82	5.89	5.17	7.82	7.32
Na_2O	2.59	4.21	2.86	4.60	3.52	4.33	1.48	3.82	3.87	3.35	4.46	4.54	4.77	4.13	4.43
K_2O	1.62	0.79	0.95	1.09	2.30	0.26	4.79	0.75	1.12	0.72	2.43	2.45	1.01	0.48	0.43
P_2O_5	0.43	0.47	0.54	0.55	0.48	0.37	0.30	0.38	0.38	0.29	0.59	0.59	0.61	0.32	0.40
LOI	2.68	3.39	2.94	2.86	2.41	3.57	3.15	3.93	3.75	3.59	2.30	1.97	3.53	2.54	3.26
Total	98.56	98.76	98.71	98.77	98.60	98.78	98.66	98.89	98.60	98.58	99.03	98.88	98.64	98.91	98.88
Mg#	40.1	42.6	41.8	33.7	38.0	46.1	41.5	48.7	49.6	48.1	31.6	31.5	36.8	44.6	44.8
Trace elements (ppm)															
Li	12.6	10.9	14.6	5.92	4.84	11.9	6.94	10.4	12.2	11.6	7.74	7.61	6.95	3.63	12.2
Be	1.44	1.82	1.52	3.88	2.45	1.19	1.39	0.97	0.90	1.20	3.13	3.12	3.09	1.56	1.68
Sc	26.8	25.6	29.9	18.7	23.9	27.9	24.6	28.6	29.3	29.3	23.0	22.8	23.6	33.9	28.4
V	302	293	312	295	321	299	312	304	323	310	318	316	338	356	258
Cr	110	65.7	81.7	6.83	58.1	108	115	124	133	144	9.65	9.85	7.88	76.5	114
Co	37.7	34.6	43.9	30.9	40.4	40.9	39.6	43.2	41.5	43.6	34.4	32.5	35.7	43.8	41.6
Ni	61.3	49.4	66.2	25.1	49.6	67.7	72.1	75.0	78.8	85.0	25.4	24.5	24.7	58.7	65.2
Cu	108	26.7	61.4	243	103	127	142	156	111	148	114	113	50.7	205	144
Zn	231	274	157	202	163	125	127	128	102	131	140	135	155	136	146
Ga	22.2	19.4	19.2	23.4	25.1	22.7	18.1	21.4	21.7	21.9	24.0	22.9	30.0	22.0	22.0
Rb	50.5	20.2	27.3	19.0	70.0	9.41	90.1	23.7	26.8	19.2	37.5	37.5	16.7	11.9	10.8
Sr	304	61.9	228	133	630	441	212	413	357	369	212	186	132	297	377
Ba	456	307	201	269	688	101	986	263	567	190	531	485	229	81.3	144
Y	33.0	32.3	36.8	41.6	34.6	30.9	26.8	28.8	29.9	27.3	40.1	39.2	40.8	30.8	30.4
Zr	188	169	210	411	309	197	168	181	181	172	388	380	404	191	187
Hf	5.12	4.74	5.85	11.3	8.55	5.53	4.71	5.13	5.07	4.89	10.5	10.2	11.1	5.33	5.37
Nb	23.6	22.0	26.9	51.9	41.8	23.7	18.9	20.5	20.7	20.0	51.6	50.3	54.1	21.8	21.4
Ta	1.69	1.64	2.00	3.75	3.09	1.7	1.42	1.52	1.56	1.49	3.82	3.69	3.97	1.61	1.62
Cs	0.89	1.18	0.96	0.18	0.056	0.27	0.26	0.51	0.39	0.25	0.12	0.13	0.045	0.45	0.25
Pb	14.2	6.72	2.39	10.0	7.90	2.24	4.45	2.61	2.12	3.58	7.15	6.99	6.77	2.15	3.02
Th	4.17	3.68	4.71	11.9	8.48	3.96	3.41	3.51	3.47	3.33	9.31	9.27	10.1	3.65	3.86
U	0.98	0.72	1.09	2.49	1.73	1.10	0.74	0.89	0.82	0.76	1.95	1.95	2.14	0.85	0.94
La	28.7	25.7	32.2	62.7	48.2	27.4	23.3	22.6	21.3	23.7	65.7	65.9	68.7	25.1	27.1
Ce	63.0	57.2	71.2	136	105	61.4	53.2	53.7	51.6	52.8	138	137	144	57.0	59.1
Pr	8.25	7.60	9.48	17.4	13.4	8.53	7.16	7.43	7.18	6.94	17.4	17.3	18.1	7.52	8.00
Nd	34.8	31.8	39.9	67.9	54.3	36.1	30.2	31.7	31.5	29.0	68.5	67.4	71.4	31.4	34.4
Sm	7.72	7.39	8.97	13.2	10.7	8.55	6.75	7.41	7.47	6.58	13.0	13.1	13.6	7.10	7.95
Eu	2.51	2.37	2.57	3.66	3.10	2.56	2.21	2.43	2.24	2.17	3.72	3.68	3.87	2.11	2.68
Gd	6.75	6.45	7.77	10.9	9.01	6.92	6.02	6.27	6.36	5.67	10.7	10.7	11.1	6.26	6.83
Tb	1.13	1.10	1.32	1.67	1.36	1.18	0.98	1.06	1.10	0.98	1.63	1.61	1.72	1.10	1.15
Dy	6.79	6.38	7.69	9.05	7.67	6.79	5.73	6.25	6.40	5.76	8.77	8.56	9.19	6.56	6.48
Ho	1.33	1.28	1.53	1.72	1.41	1.30	1.12	1.22	1.24	1.14	1.64	1.65	1.74	1.30	1.28
Er	3.51	3.34	4.02	4.42	3.71	3.37	2.97	3.19	3.30	2.98	4.34	4.23	4.49	3.44	3.38
Tm	0.46	0.44	0.52	0.55	0.47	0.43	0.38	0.41	0.42	0.39	0.53	0.52	0.56	0.45	0.43
Yb	3.01	2.81	3.36	3.52	2.98	2.83	2.47	2.68	2.73	2.63	3.48	3.45	3.67	2.98	2.78
Lu	0.41	0.38	0.47	0.47	0.40	0.42	0.34	0.39	0.38	0.36	0.48	0.47	0.49	0.41	0.39

HK-53	HK-60	HK-61	HK-62	HK-63	HK-64	HK-65	HK-5	HK-40	HK-41	HK-92	HK-1	HK-2	HK-4	HK-6	HK-17
B–C	C	C	C	C	C	C	E	B–C	B–C	D	E	E	E	E	B
							Low-Ti picrites				Low-Ti basalts				
47.68	43.39	45.52	45.10	45.28	46.22	45.52	46.21	43.96	43.96	46.75	48.65	49.05	49.38	47.58	47.20
2.77	3.25	3.29	3.33	3.30	3.46	3.31	0.84	0.67	0.74	0.59	0.92	1.71	0.76	0.84	0.54
13.10	13.91	13.85	14.54	14.10	12.44	13.63	10.24	11.28	11.21	13.39	13.92	14.44	12.45	11.69	12.40
13.15	14.82	15.22	14.76	13.83	14.77	14.00	10.64	11.29	11.37	11.10	10.45	12.04	9.79	10.19	10.12
0.20	0.27	0.25	0.21	0.26	0.23	0.23	0.16	0.17	0.17	0.16	0.14	0.19	0.18	0.16	0.14
6.23	5.72	4.70	4.45	4.73	4.98	4.51	14.80	16.71	16.06	13.45	8.87	6.00	10.56	11.94	8.87
7.51	9.70	9.47	10.60	11.04	7.84	9.35	9.36	9.45	9.81	8.39	6.70	9.77	8.43	9.15	13.90
4.37	2.88	2.77	2.66	2.44	3.51	2.63	1.70	1.06	1.06	2.12	3.70	2.19	3.22	2.68	2.45
0.34	0.89	1.26	1.20	1.26	1.18	1.78	0.28	0.05	0.05	0.11	1.64	1.54	0.39	0.36	0.07
0.39	0.72	0.71	0.67	0.63	0.74	0.70	0.15	0.05	0.06	0.04	0.19	0.19	0.12	0.17	0.03
3.04	3.20	1.75	1.54	1.96	3.18	3.06	5.15	4.07	4.54	3.06	3.46	2.68	3.36	3.92	3.94
98.78	98.75	98.79	99.07	98.82	98.55	98.72	99.53	98.75	99.01	99.16	98.64	99.80	98.64	98.67	99.68
45.8	40.8	35.5	35.0	37.9	37.5	36.5	71.3	72.5	71.6	68.3	60.2	47.0	65.8	67.6	61.0
11.7	6.36	8.26	7.12	9.40	8.54	11.7	15.5	4.82	4.71	11.0	13.4	8.72	10.5	14.5	2.19
1.13	0.92	1.24	1.17	1.17	1.62	1.56	0.92	0.14	0.16	0.24	1.44	0.94	1.00	1.07	0.12
28.2	27.5	25.3	27.3	26.2	24.8	24.7	35.3	32.5	32.7	42.1	35.9	34.8	36.6	34.4	36.6
299	260	282	268	253	257	311	211	229	251	253	221	238	214	218	163
116	71.2	44.3	49.2	47.6	18.6	38.9	993	999	981	711	380	219	816	781	527
42.9	50.0	48.0	47.4	43.3	40.1	39.5	65.7	76.1	74.1	64.5	51.6	42.5	56.4	56.8	47.3
68.7	75.9	45.5	47.5	45.6	26.6	39.6	371	548	526	355	211	84.5	280	270	229
135	129	95.1	93.6	95.9	110	106	88.1	114	125	47.9	102	195	58.0	89.3	42.3
133	147	152	153	140	163	167	83.2	81.9	84.1	86.9	99.6	110	82.7	103	58.3
20.0	21.8	21.6	23.7	22.5	21.7	23.3	12.1	13.1	13.1	14.1	17.4	21.1	15.5	14.7	12.8
9.4	22.6	17.9	12.7	12.8	18.8	25.4	6.42	2.73	2.15	2.52	60.2	65.1	14.3	11.0	1.44
316	463	515	529	556	357	827	52.0	56.7	72.2	79.6	167	203	210	166	110
130	530	750	707	677	369	1204	48.7	7.0	10.0	28.4	379	170	119	94.3	15.3
29.1	26.9	29.5	29.4	29.2	40.6	38.0	15.3	15.5	17.0	15.0	25.1	28.9	20.3	18.7	15.1
185	153	163	162	163	220	204	59.9	29.4	35.9	20.9	121	116	90.4	90.4	20.8
5.28	4.31	4.65	4.63	4.61	6.09	5.73	1.82	1.00	1.17	0.74	3.50	3.37	2.57	2.66	0.73
21.7	22.4	24.3	23.8	23.7	33.8	30.8	5.98	0.66	0.76	0.87	16.9	7.04	7.93	7.13	0.37
1.61	1.68	1.79	1.76	1.77	2.45	2.24	0.42	0.060	0.066	0.078	1.11	0.52	0.60	0.54	0.039
0.15	0.32	0.28	0.29	0.98	0.21	0.27	1.34	1.20	1.03	0.053	1.12	1.27	1.39	1.00	0.12
2.15	3.02	3.12	2.94	2.80	2.87	2.48	2.74	0.57	0.63	1.32	6.33	2.95	4.05	4.94	0.64
3.82	3.47	3.52	3.43	3.43	5.54	5.15	2.84	0.046	0.11	0.20	6.04	2.65	4.64	4.64	0.033
0.91	0.62	0.89	0.85	0.82	1.33	1.17	0.45	0.012	0.015	0.044	1.29	0.71	0.81	0.78	0.006
25.2	30.8	34.4	32.6	33.2	45.0	46.3	5.94	0.76	0.87	1.05	19.7	9.62	13.5	11.6	0.60
58.4	68.6	76.4	73.4	74.1	103	100	13.8	2.50	2.82	2.83	40.6	22.2	28.4	24.8	1.78
7.90	9.43	10.3	10.0	10.1	14.0	13.6	1.81	0.49	0.56	0.47	4.84	3.10	3.44	2.99	0.35
34.1	40.9	45.1	43.4	43.5	59.3	57.9	7.76	3.09	3.57	2.67	18.1	14.4	13.2	11.8	2.28
7.69	8.47	9.31	9.05	9.16	12.5	11.7	2.04	1.48	1.67	1.10	4.01	4.27	2.91	2.86	1.12
2.62	3.40	3.43	3.51	3.61	3.62	3.91	0.51	0.64	0.70	0.53	0.91	1.45	0.87	0.73	0.57
6.59	6.98	7.81	7.54	7.49	10.2	9.78	2.09	1.81	1.97	1.50	3.80	4.31	2.88	2.73	1.43
1.10	1.10	1.21	1.18	1.17	1.63	1.53	0.43	0.40	0.45	0.34	0.71	0.85	0.54	0.52	0.35
6.40	6.17	6.65	6.55	6.53	9.12	8.63	2.89	2.90	3.22	2.62	4.58	5.53	3.63	3.45	2.63
1.24	1.18	1.28	1.26	1.25	1.75	1.65	0.63	0.64	0.71	0.61	1.00	1.14	0.77	0.75	0.60
3.23	3.00	3.27	3.23	3.25	4.51	4.21	1.75	1.78	1.97	1.71	2.84	3.08	2.22	2.11	1.65
0.42	0.38	0.41	0.42	0.41	0.57	0.53	0.25	0.25	0.27	0.24	0.40	0.41	0.31	0.30	0.24
2.74	2.43	2.64	2.57	2.68	3.68	3.46	1.73	1.70	1.84	1.69	2.80	2.73	2.21	2.08	1.63
0.37	0.33	0.38	0.36	0.36	0.51	0.47	0.26	0.24	0.26	0.24	0.39	0.39	0.33	0.31	0.23

(continued on next page)

Table 1 (*continued*)

Samples	HK-30	HK-47	HK-48	HK-49	HK-50	HK-51	HK-59	HK-85	HK-87	HK-89	HK-90	HK-93	HK-94	HK-95
Sites	B	B–C	B–C	B–C	B–C	B–C	B–C	D	D	D	D	D	D	D
Rock types	Low-Ti basalts													
Major oxides (wt.%)														
SiO_2	46.45	50.36	50.23	51.08	51.02	50.36	46.78	47.15	47.45	47.44	48.50	48.45	51.07	49.30
TiO_2	2.12	1.02	1.03	1.00	1.00	1.00	2.36	1.26	1.30	1.37	1.22	0.75	0.77	1.47
Al_2O_3	13.60	15.86	15.53	15.25	15.51	15.32	14.42	15.03	13.60	13.71	15.74	11.89	11.00	13.56
$Fe_2O_3(t)$	13.28	9.94	9.76	9.64	9.70	9.85	12.48	11.33	10.53	10.97	11.38	9.55	9.35	11.24
MnO	0.19	0.15	0.16	0.16	0.15	0.16	0.17	0.16	0.17	0.17	0.20	0.15	0.17	0.15
MgO	5.79	5.85	5.81	5.74	5.87	5.80	5.95	7.69	8.06	6.07	5.98	10.69	10.58	7.53
CaO	10.30	6.26	6.87	6.27	6.59	7.39	8.87	10.83	12.62	13.22	8.72	11.82	12.20	8.56
Na_2O	3.49	4.84	4.78	4.78	5.11	4.43	3.35	1.18	1.43	2.22	3.90	2.94	3.17	2.40
K_2O	0.21	0.59	0.37	0.88	0.30	0.70	1.28	0.92	0.31	0.45	0.39	0.03	0.02	2.24
P_2O_5	0.20	0.11	0.11	0.11	0.11	0.11	0.32	0.14	0.10	0.15	0.16	0.17	0.17	0.36
LOI	3.02	3.79	3.84	3.64	3.69	3.93	2.82	2.91	3.17	3.02	2.76	2.85	2.39	2.97
Total	98.64	98.78	98.51	98.54	99.06	99.06	98.80	98.60	98.73	98.78	98.96	99.28	100.90	99.78
Mg#	43.7	51.2	51.5	51.5	51.9	51.2	46.0	54.8	57.7	49.7	48.4	66.6	66.8	54.4
Trace elements (ppm)														
Li	7.98	2.95	2.54	2.33	2.25	2.87	9.71	18.7	16.0	22.4	10.1	4.77	4.62	8.71
Be	1.44	1.54	1.26	1.24	1.30	1.32	1.51	1.10	0.74	1.20	1.50	1.07	1.47	1.13
Sc	35.2	36.8	37.8	36.5	37.8	37.3	27.2	37.6	35.6	28.0	32.7	41.3	38.8	33.0
V	310	225	230	223	222	228	281	297	289	258	270	258	233	246
Cr	166	250	243	246	242	246	172	170	84.0	45.0	82.3	534	543	254
Co	45.0	28.8	29.1	28.1	28.6	28.5	42.5	39.3	45.1	34.2	39.9	52.1	51.1	45.4
Ni	64.4	5.89	5.45	6.00	6.49	5.67	89.8	35.6	47.7	17.9	52.1	219	235	60.2
Cu	218	16.7	406	24.2	20.6	91.4	147	37.7	41.8	14.7	62.2	189	107	63.7
Zn	131	81.6	80.9	88.8	85.6	83.5	131	107	79.1	80.8	114	84.6	71.5	118
Ga	20.1	17.6	18.6	18.2	18.0	19.2	21.5	20.4	17.5	18.6	19.5	13.8	10.7	16.6
Rb	4.86	22.8	14.6	27.4	12.3	21.7	41.5	34.1	8.75	19.0	8.84	0.72	0.70	21.9
Sr	364	178	149	137	155	147	518	211	265	237	116	138	77.5	365
Ba	87.8	86.8	50.8	154	45.9	178	226	155	77.9	89.5	123	76.3	47.6	816
Y	30.4	26.0	26.6	25.4	25.4	25.7	29.1	23.1	18.5	23.5	27.4	14.2	14.0	18.9
Zr	157	111	114	109	110	111	191	89.8	66.9	96.1	122	35.5	37.5	100
Hf	4.39	3.38	3.43	3.30	3.35	3.43	5.38	2.66	1.97	2.83	3.50	1.15	1.17	2.96
Nb	15.2	8.03	8.11	7.87	7.96	7.91	22.3	8.96	7.26	9.52	10.7	5.68	5.68	18.2
Ta	1.10	0.69	0.70	0.68	0.70	0.70	1.68	0.63	0.51	0.70	0.74	0.36	0.37	1.18
Cs	0.046	0.33	0.17	0.22	0.22	0.28	0.37	1.16	0.43	1.65	0.044	0.15	0.15	0.18
Pb	4.65	3.68	3.13	3.44	4.04	2.78	3.48	3.77	2.93	3.68	3.71	1.89	1.40	1.84
Th	3.43	6.82	7.26	6.98	7.04	7.42	4.22	2.67	1.79	3.01	3.66	1.01	1.04	2.15
U	0.82	1.17	1.23	1.13	1.17	1.31	1.04	0.62	0.56	0.77	0.66	0.23	0.23	0.58
La	23.9	20.3	19.7	19.0	19.8	19.9	26.5	14.8	9.22	13.5	20.0	3.85	3.82	18.3
Ce	49.1	42.1	41.9	40.2	41.3	41.0	59.1	29.4	19.6	28.2	40.5	7.90	7.99	38.4
Pr	6.34	4.98	5.10	4.86	4.97	4.92	7.77	3.68	2.50	3.68	4.93	1.15	1.12	4.83
Nd	26.0	19.4	19.9	19.1	19.3	19.4	32.9	15.9	10.6	15.4	19.9	5.06	4.85	20.1
Sm	5.88	4.43	4.55	4.34	4.36	4.45	7.30	4.11	2.90	3.81	4.62	1.54	1.54	4.75
Eu	1.91	1.20	1.15	1.13	1.16	1.18	2.25	1.13	1.06	1.22	1.42	0.62	0.44	1.52
Gd	5.37	4.22	4.36	4.14	4.20	4.20	6.25	3.86	2.83	3.68	4.31	1.75	1.71	4.20
Tb	0.98	0.77	0.80	0.77	0.77	0.77	1.06	0.73	0.57	0.71	0.81	0.37	0.37	0.70
Dy	6.13	5.00	5.18	4.98	5.03	5.01	6.42	4.56	3.69	4.48	5.18	2.63	2.63	4.12
Ho	1.25	1.06	1.09	1.06	1.07	1.07	1.25	0.92	0.75	0.96	1.10	0.59	0.55	0.77
Er	3.39	2.98	3.11	2.97	2.99	3.05	3.26	2.58	1.99	2.58	3.03	1.69	1.56	2.05
Tm	0.46	0.42	0.44	0.41	0.42	0.42	0.44	0.35	0.28	0.36	0.44	0.24	0.23	0.28
Yb	3.12	2.86	2.96	2.82	2.89	2.87	2.81	2.24	1.86	2.34	2.96	1.66	1.52	1.86
Lu	0.43	0.42	0.43	0.41	0.41	0.41	0.40	0.31	0.26	0.33	0.42	0.23	0.23	0.26

HK-96	HK-97	HK-98	HK-99	JP-3	JP-4	JP-5	JP-6	JP-7	JP-8	JP-9	JP-10	JP-16	JP-19	JP-21-1	JP-21-2	JP-22
D	D	D	D	A	A	A	A	A	A	A	A	A	A	A	A	A
46.43	50.82	52.57	51.18	50.66	49.87	50.38	47.93	47.71	48.08	49.54	46.41	45.48	52.23	50.43	50.92	48.21
1.60	1.16	1.01	1.26	2.19	2.45	2.46	2.45	1.76	1.88	1.44	1.20	1.87	1.69	1.46	1.41	1.33
15.34	12.49	13.95	12.50	11.61	12.46	12.38	12.21	13.98	12.59	13.61	14.17	13.83	15.20	14.57	14.51	15.22
11.76	10.84	10.04	11.85	16.04	11.28	11.08	16.60	12.78	14.70	11.30	11.75	13.21	10.46	10.37	10.34	10.14
0.18	0.17	0.15	0.17	0.16	0.15	0.15	0.23	0.18	0.22	0.17	0.20	0.19	0.18	0.17	0.16	0.16
7.10	8.57	6.54	9.66	3.83	6.87	6.99	5.22	7.42	6.43	8.16	8.28	7.26	5.49	5.72	5.69	5.48
10.44	12.13	10.51	9.46	6.32	8.49	7.71	9.96	6.61	8.05	6.59	11.09	10.97	5.11	8.28	6.58	11.64
2.77	1.47	2.47	1.80	5.42	3.36	3.90	2.39	4.39	4.18	4.39	2.40	2.47	4.76	4.12	3.80	2.96
0.75	0.20	0.10	0.49	1.00	1.46	0.88	0.54	0.70	0.55	0.55	0.72	1.11	0.71	0.46	2.28	0.43
0.21	0.16	0.19	0.15	0.30	0.29	0.29	0.31	0.26	0.30	0.16	0.15	0.35	0.24	0.23	0.22	0.22
2.61	2.45	3.72	1.95	1.66	3.02	3.51	1.96	4.04	2.75	4.18	3.34	3.09	3.44	3.55	3.14	3.57
99.19	100.46	101.25	100.45	99.18	99.72	99.73	99.80	99.82	99.72	100.11	99.71	99.83	99.50	99.36	99.06	99.35
51.8	58.5	53.7	59.2	29.9	52.1	52.9	35.9	50.9	43.8	56.3	55.7	49.5	48.3	49.6	49.5	49.1
11.6	4.34	3.04	5.11	6.40	11.7	15.2	12.2	16.9	11.4	11.5	15.5	9.68	6.71	8.22	7.92	10.9
1.38	0.99	1.52	0.87	1.30	1.57	1.25	0.99	1.12	0.93	0.55	0.65	1.09	1.61	0.96	0.82	1.13
33.3	32.8	28.3	32.4	33.7	30.4	31.3	34.9	31.7	33.9	29.5	40.3	30.6	29.2	29.3	28.5	27.8
303	253	226	250	310	279	289	442	332	373	229	283	372	272	234	230	231
159	381	110	349	22.0	268	272	23.4	129	60.0	440	258	78.1	104	333	350	338
44.7	50.6	39.7	54.3	34.7	41.4	39.9	50.9	43.8	52.9	48.7	53.3	50.9	36.2	37.4	37.9	37.2
74.3	42.8	19.6	88.6	43.7	34.9	29.1	42.1	74.7	57.9	47.9	120	83.6	38.4	16.2	14.0	18.2
80.2	57.9	35.1	62.8	424	48.9	48.5	313	397	62.4	55.0	237	204	25.8	7.9	7.6	14.4
117	95.1	87.9	111	77.2	112	106	149	250	124	106	88.9	120	93.0	84.9	94.7	84.6
23.7	19.3	18.7	17.9	13.0	20.7	20.5	21.7	20.9	14.9	17.3	15.9	18.9	22.0	18.7	15.0	21.2
15.7	4.93	2.28	12.1	11.3	28.2	14.1	9.18	7.71	9.07	8.74	20.7	30.0	20.3	10.9	64.2	9.52
206	427	413	206	45.3	284	215	215	95.8	280	85.9	312	227	315	91	213	71.7
158	107	48.2	180	66.2	613	348	185	166	245	120	202	361	194	104	1391	116
28.4	18.4	18.7	21.1	32.4	30.3	30.1	36.7	27.1	27.4	17.4	21.1	23.6	28.9	24.0	23.2	22.0
139	84.2	121	107	139	220	223	160	111	111	92.5	67.5	96.5	215	125	120	115
4.06	2.50	3.41	3.16	3.72	5.41	5.67	4.18	2.87	2.93	2.45	1.91	2.70	5.62	3.42	3.22	3.11
11.4	6.90	10.6	7.85	14.0	21.2	21.7	15.5	10.6	11.7	6.85	8.95	11.1	15.1	11.5	11.1	10.1
0.83	0.52	0.73	0.57	0.83	1.35	1.39	0.93	0.64	0.69	0.47	0.55	0.68	1.03	0.72	0.70	0.65
0.10	0.28	0.073	0.27	0.22	0.63	0.30	0.66	0.26	0.50	0.37	0.68	2.25	0.85	0.64	1.25	0.46
5.50	4.10	6.39	3.61	2.01	2.56	2.05	2.90	4.44	4.50	2.49	5.60	2.45	3.51	0.80	0.87	2.09
5.08	1.71	3.61	3.25	1.58	5.88	5.97	1.80	1.25	1.24	1.63	1.13	0.91	7.90	3.42	3.26	3.08
1.27	0.39	0.84	0.71	0.26	1.40	1.53	0.52	0.31	0.30	0.39	0.22	0.22	1.82	0.71	0.69	0.64
19.1	11.6	16.1	15.6	11.1	31.9	33.8	13.9	10.4	9.18	9.50	8.53	8.27	27.3	15.9	15.2	14.9
40.9	23.8	33.4	31.6	27.9	69.6	71.7	32.8	23.4	22.6	22.9	17.6	19.4	56.4	34.6	33.0	32.5
5.23	3.11	4.08	4.01	3.97	8.78	9.06	4.59	3.26	3.28	3.18	2.28	2.83	6.97	4.52	4.30	4.13
21.4	13.3	16.2	16.7	18.3	37.0	37.2	21.4	15.2	15.0	14.1	10.2	13.4	28.2	19.2	18.4	17.4
5.48	3.42	3.63	4.03	4.97	7.72	7.85	5.74	4.07	4.07	3.34	2.85	3.80	6.20	4.51	4.38	4.22
1.68	1.22	1.15	1.18	1.67	2.11	2.17	1.92	1.39	1.42	1.17	1.04	1.44	1.72	1.55	1.34	1.43
5.09	3.20	3.37	3.78	5.26	6.90	6.99	5.99	4.33	4.45	3.36	3.20	4.20	5.84	4.53	4.48	4.29
0.92	0.57	0.60	0.69	1.01	1.15	1.16	1.13	0.83	0.86	0.60	0.63	0.79	1.00	0.84	0.79	0.76
5.75	3.65	3.66	4.24	6.06	6.05	6.21	6.91	5.10	5.22	3.49	3.98	4.72	5.57	4.80	4.62	4.45
1.17	0.73	0.75	0.87	1.26	1.18	1.20	1.43	1.05	1.09	0.72	0.83	0.95	1.13	0.98	0.92	0.90
3.15	2.00	2.07	2.37	3.46	3.19	3.20	3.99	2.97	3.03	1.95	2.40	2.59	3.09	2.64	2.53	2.49
0.44	0.26	0.29	0.31	0.49	0.44	0.44	0.57	0.42	0.44	0.27	0.34	0.37	0.44	0.37	0.34	0.34
2.83	1.82	1.94	2.06	3.08	2.57	2.60	3.50	2.52	2.71	1.66	2.12	2.14	2.72	2.27	2.19	2.06
0.41	0.26	0.27	0.30	0.45	0.38	0.38	0.52	0.39	0.41	0.25	0.33	0.33	0.41	0.33	0.33	0.32

Table 2
Major and trace elements of the mafic intrusions in the Jinping–Song Da district

Samples	JP-11	JP-12	JP-13	JP-14	HK-67	HK-69	HK-70	HK-72	HK-73	HK-76	HK-80
Sites	A	A	A	A	D	D	D	D	D	D	C–D
Rock types	High-Ti gabbro				Low-Ti olivine gabbro						
Major oxides (wt.%)											
SiO_2	47.13	48.39	46.44	46.66	43.45	45.77	44.37	45.59	46.27	48.07	41.94
TiO_2	3.70	3.53	3.70	3.86	0.57	0.76	0.69	0.73	0.77	0.74	0.87
Al_2O_3	13.65	14.24	13.44	13.97	6.73	8.37	8.49	8.30	8.44	8.92	8.93
Fe_2O_3(t)	13.12	13.17	14.36	13.76	11.41	11.38	12.06	10.99	10.46	10.48	13.18
MnO	0.19	0.19	0.19	0.20	0.17	0.19	0.18	0.17	0.16	0.17	0.20
MgO	5.52	4.89	5.40	5.27	26.63	19.46	21.64	19.71	19.11	15.23	20.63
CaO	9.30	9.03	8.53	8.68	7.04	10.45	8.86	10.72	11.22	14.05	7.78
Na_2O	2.41	2.64	2.99	2.86	0.69	0.85	0.93	0.87	0.98	0.94	0.22
K_2O	1.60	1.84	1.82	1.93	0.32	0.40	0.24	0.30	0.32	0.29	0.07
P_2O_5	0.42	0.45	0.46	0.40	0.07	0.08	0.07	0.07	0.08	0.06	0.14
LOI	2.14	1.68	2.30	2.02	1.62	1.38	1.02	1.26	0.93	0.44	4.79
Total	99.17	100.05	99.65	99.62	98.72	99.08	98.53	98.72	98.75	99.40	98.75
Mg#	42.9	39.8	40.1	40.6	80.6	75.3	76.2	76.2	76.5	72.1	73.6
Trace elements (ppm)											
Li	7.83	6.78	10.9	7.82	14.4	8.76	7.47	13.4	12.4	6.91	9.36
Be	1.75	1.94	1.90	1.70	0.39	0.40	0.32	0.37	0.47	0.28	0.64
Sc	27.3	24.9	26.4	26.8	23.6	35.0	28.5	34.6	39.8	52.3	19.0
V	376	340	397	383	152	219	197	214	244	285	183
Cr	128	99.4	45.5	93.7	1865	1356	1712	1362	1481	2128	1386
Co	45.8	42.1	47.5	45.1	102	82.7	95.8	80.1	81.9	67.2	92.4
Ni	85.7	73.5	61.6	75.0	1022	643	748	612	629	380	868
Cu	225	245	261	210	54.3	71.8	78.0	55.5	74.1	67.9	610
Zn	134	137	138	134	92.6	105	96.3	90.3	84.6	83.8	106
Ga	21.8	23.2	22.6	21.9	9.35	11.3	11.4	10.9	11.8	11.7	12.2
Rb	35.1	41.5	49.1	46.5	10.6	14.7	6.86	9.35	10.2	11.0	0.80
Sr	540	562	499	518	92.5	98.6	90.7	108	106	94.2	37.7
Ba	453	496	715	510	83.7	104	57.8	98.2	82.5	79.9	7.13
Y	27.5	29.8	29.5	26.6	10.2	12.8	12.1	12.1	13.7	13.6	13.2
Zr	276	312	292	266	42.9	42.8	40.1	39.0	48.8	38.9	51.3
Hf	6.78	7.63	7.18	6.56	1.29	1.33	1.25	1.24	1.55	1.28	1.52
Nb	37.9	40.1	38.7	35.8	3.34	3.36	3.04	3.12	3.82	2.74	3.62
Ta	2.43	2.68	2.57	2.36	0.24	0.25	0.22	0.22	0.26	0.20	0.26
Cs	0.48	0.56	0.72	0.63	0.64	1.54	0.75	1.05	0.63	0.86	0.25
Pb	4.98	6.94	5.25	4.22	3.10	3.73	2.30	5.10	3.80	6.52	1.38
Th	4.74	5.47	4.98	4.48	1.38	1.12	0.89	0.96	1.32	0.91	0.82
U	1.17	1.36	1.19	1.08	0.33	0.27	0.23	0.22	0.30	0.22	0.20
La	39.8	44.4	44.0	38.0	5.14	5.00	4.12	4.47	5.73	4.27	4.17
Ce	85.3	93.5	94.4	82.1	11.0	10.9	9.18	9.73	12.5	9.58	10.1
Pr	10.7	12.0	11.6	10.2	1.44	1.47	1.28	1.33	1.68	1.34	1.47
Nd	43.8	47.9	47.3	41.8	6.24	6.73	5.81	6.20	7.39	6.37	6.89
Sm	8.30	8.92	9.04	8.03	1.60	1.91	1.76	1.77	2.16	1.95	2.19
Eu	2.51	2.68	2.84	2.50	0.53	0.67	0.62	0.64	0.73	0.65	0.71
Gd	7.23	7.75	7.87	6.92	1.61	1.92	1.81	1.77	2.08	2.06	2.04
Tb	1.14	1.22	1.22	1.06	0.31	0.39	0.36	0.36	0.42	0.38	0.40
Dy	5.91	6.44	6.40	5.72	2.03	2.53	2.36	2.48	2.73	2.64	2.66
Ho	1.14	1.21	1.23	1.09	0.43	0.54	0.50	0.52	0.59	0.56	0.55
Er	3.07	3.25	3.19	2.92	1.16	1.48	1.40	1.40	1.59	1.54	1.57
Tm	0.40	0.45	0.44	0.39	0.17	0.20	0.19	0.19	0.21	0.21	0.21
Yb	2.49	2.69	2.62	2.39	1.07	1.32	1.26	1.27	1.45	1.38	1.35
Lu	0.36	0.40	0.39	0.35	0.16	0.19	0.18	0.18	0.21	0.20	0.20

HK-81	HK-84	HK-71	HK-74	HK-77	HK-86	JP-25	JP-26	JP-27	JP-28
C–D	C–D	D	D	D	D	A	A	A	A
		Low-Ti gabbro							
42.72	42.95	46.91	47.84	48.92	47.81	45.86	47.39	47.49	48.07
0.71	0.82	1.00	0.97	1.54	0.94	0.66	1.81	0.93	0.56
8.07	8.17	12.37	12.05	14.47	13.49	12.00	13.76	13.28	10.03
12.22	15.01	11.07	11.36	13.42	10.41	10.26	12.79	9.28	9.77
0.15	0.21	0.25	0.18	0.22	0.16	0.16	0.15	0.14	0.14
21.64	22.24	10.84	12.25	6.31	9.72	14.29	9.85	11.51	15.21
6.78	5.66	12.77	12.69	9.96	10.70	11.70	6.59	11.82	12.97
0.18	0.17	1.35	1.44	2.08	0.83	0.89	0.33	1.91	0.97
0.05	0.04	0.53	0.32	0.90	0.79	0.58	0.30	0.89	0.40
0.10	0.12	0.10	0.09	0.18	0.09	0.09	0.40	0.14	0.12
6.56	3.27	1.49	0.36	0.79	4.08	2.50	6.32	2.59	1.40
99.18	98.67	98.69	99.56	98.80	99.01	98.98	99.69	99.99	99.65
75.9	72.5	63.6	65.8	45.6	62.5	71.3	57.8	68.9	73.5
5.66	5.26	36.6	8.09	13.3	17.4	18.1	62.4	23.9	15.4
0.81	0.57	0.50	0.46	1.24	0.75	0.38	1.31	0.62	0.64
20.4	20.7	39.2	38.4	37.2	32.2	34.0	21.3	38.7	39.9
167	157	270	265	268	237	236	176	295	275
1596	1626	755	869	79.1	129	204	314	422	174
77.2	85.3	57.6	62.3	49.2	46.8	60.6	50.9	41.4	66.7
820	1187	230	283	22.0	59.1	99.5	196.2	43.1	67.3
18.1	113	102	105	35.1	29.7	86.7	45.0	33.7	22.9
89.9	95.4	108	100	134	125	75.2	98.2	51.8	67.7
12.1	12.0	16.5	15.3	22.3	16.5	12.3	19.4	16.3	11.7
0.45	0.38	22.3	10.0	34.2	24.7	21.6	11.6	63.0	12.8
30.6	26.1	233	132	163	181	281	772	371	232
2.52	2.24	158	82.4	202	160	136	238	162	135
12.1	14.8	17.9	16.7	34.6	17.2	11.3	20.7	15.4	17.7
42.6	40.2	57.1	52.2	147	68.4	41	115	60.0	85.1
1.25	1.20	1.77	1.67	4.17	2.08	1.17	2.77	1.67	2.35
2.91	3.40	4.40	4.10	10.3	6.54	3.32	19.2	4.99	5.75
0.21	0.21	0.33	0.30	0.76	0.49	0.21	1.07	0.31	0.34
0.14	0.16	0.80	0.60	1.18	0.67	2.20	0.54	6.61	1.53
0.95	0.94	9.91	4.87	5.39	3.43	1.66	3.77	5.10	2.25
0.74	0.59	1.29	1.13	4.52	2.05	0.97	1.62	1.39	2.17
0.26	0.24	0.36	0.27	0.83	0.46	0.23	0.43	0.41	0.49
1.82	2.22	6.34	5.31	18.5	8.27	6.76	18.5	9.59	13.0
5.78	6.47	13.7	12.1	40.0	18.0	14.0	35.5	20.8	28.6
0.95	1.06	1.89	1.70	5.03	2.38	1.88	4.56	2.72	3.62
4.92	5.42	8.75	7.76	20.5	10.2	8.44	19.9	12.2	15.1
1.67	1.93	2.75	2.30	5.28	2.63	2.03	4.68	2.98	3.50
0.64	0.57	0.97	0.86	1.62	0.86	0.84	1.78	1.14	0.81
1.74	1.98	2.70	2.43	5.13	2.64	2.07	4.63	2.93	3.36
0.36	0.43	0.54	0.50	0.99	0.50	0.38	0.79	0.51	0.61
2.37	2.89	3.55	3.29	6.47	3.23	2.22	4.30	3.06	3.51
0.51	0.61	0.76	0.70	1.38	0.70	0.45	0.81	0.64	0.70
1.40	1.69	2.07	1.85	3.97	1.91	1.23	2.10	1.72	1.96
0.19	0.23	0.28	0.25	0.55	0.26	0.18	0.27	0.24	0.29
1.29	1.53	1.92	1.76	3.79	1.76	1.06	1.62	1.48	1.68
0.18	0.21	0.27	0.24	0.54	0.25	0.16	0.23	0.22	0.26

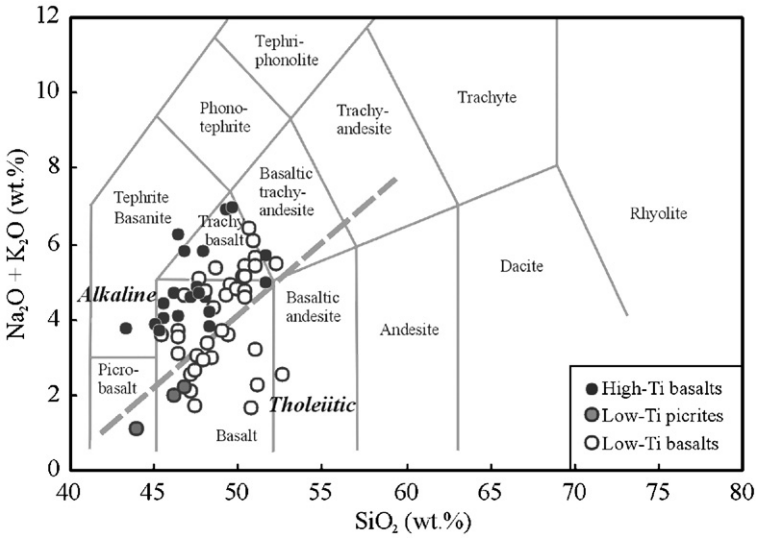

Fig. 2. Total alkalis–silica (TAS) diagram comparing the geochemical characteristics in the high-Ti and low-Ti basalts and mafic intrusions. The bold dashed line distinguishes tholeiitic from alkaline basalts (from MacDonald and Katsura, 1964).

are 36 small differentiated mafic–ultramafic intrusions with a total exposure area of ~1.5 km^2. The largest intrusion has a surface exposure of about 0.25 km^2 (Wang et al., 2006). In the Ta Khoa and Nam Muoi River regions, there are mafic–ultramafic dykes and lenticular to stock-like intrusions. The Baimazhai intrusion in Jinping and the Ban Phuc intrusion in northern Vietnam host Ni–Cu–(PGE) sulfide ore deposits (Glotov et al., 2001; Wang et al., 2006; Wang and Zhou, 2006).

The Baimazhai intrusion was dated at 258.5±3.5 Ma (Wang et al., 2006). Basaltic rocks in the Nam Muoi region have a Rb–Sr isochron age of 257±24 Ma (Polyakov et al., 1998). These ages are comparable to other published ages for the ELIP (Zhou et al., 2002; Guo et al., 2004; Zhou et al., 2005, 2006) and suggest that all these rocks were produced by a major event that formed the ELIP.

3. Petrography

According to the classification of Xu et al. (2001), the rocks of the ELIP in the Jinping–Song Da district belong to either the high-Ti or low-Ti series. The high-Ti series (TiO_2 > 2.5 wt.% and Ti/Y > 500) includes high-Ti basalts and gabbros, whereas the low-Ti series (TiO_2 < 2.5 wt.% and Ti/Y < 500) comprises low-Ti picrites, basalts, olivine gabbros and gabbros.

The high-Ti basalts are composed of plagioclase (55–65%), clinopyroxene (30–35%), magnetite + ilmenite (5–10%) and biotite (<5%). They typically have intergranular to intersertal textures, depending on the grain size. Most of lavas are aphyric but a few have sparse plagioclase phenocrysts. Interstitial material in the groundmass consists of variable proportions of deep brown glass (partly devitrified), fine-grained magnetite and small clots of clinopyroxene. Needle-like grains of ilmenite are associated with magnetite in some samples.

The high-Ti gabbros are composed of plagioclase (~55%), clinopyroxene (~35%), magnetite + ilmenite (<10%), and minor biotite and apatite (<3%). Abundant acicular grains of ilmenite (>10%) are present in a few samples. Most of the gabbros have subophitic textures, in which the plagioclase is partly or completely enclosed by clinopyroxene.

The low-Ti picrites are porphyritic and commonly amygdaloidal. Olivine phenocrysts are granular to elongate, with length/width ratios up to 9:1. All olivine grains are Mg-rich, generally ranging from Fo_{80} to Fo_{85} (our unpublished data), with some grains up to Fo_{92} (Hanski et al., 2004). Clinopyroxene phenocrysts are commonly elongated. The groundmass is typically holocrystalline, consisting mainly of clinopyroxene and plagioclase, some of which form subophitic intergrowths. In a few samples, the groundmass consists of devitrified glass with minute needles of clinopyroxene.

Most of the low-Ti basalts are porphyritic, with phenocrysts of clinopyroxene (20%), olivine (<10%) and minor plagioclase. The fine-grained groundmass has intergranular to intersertal textures, and is composed

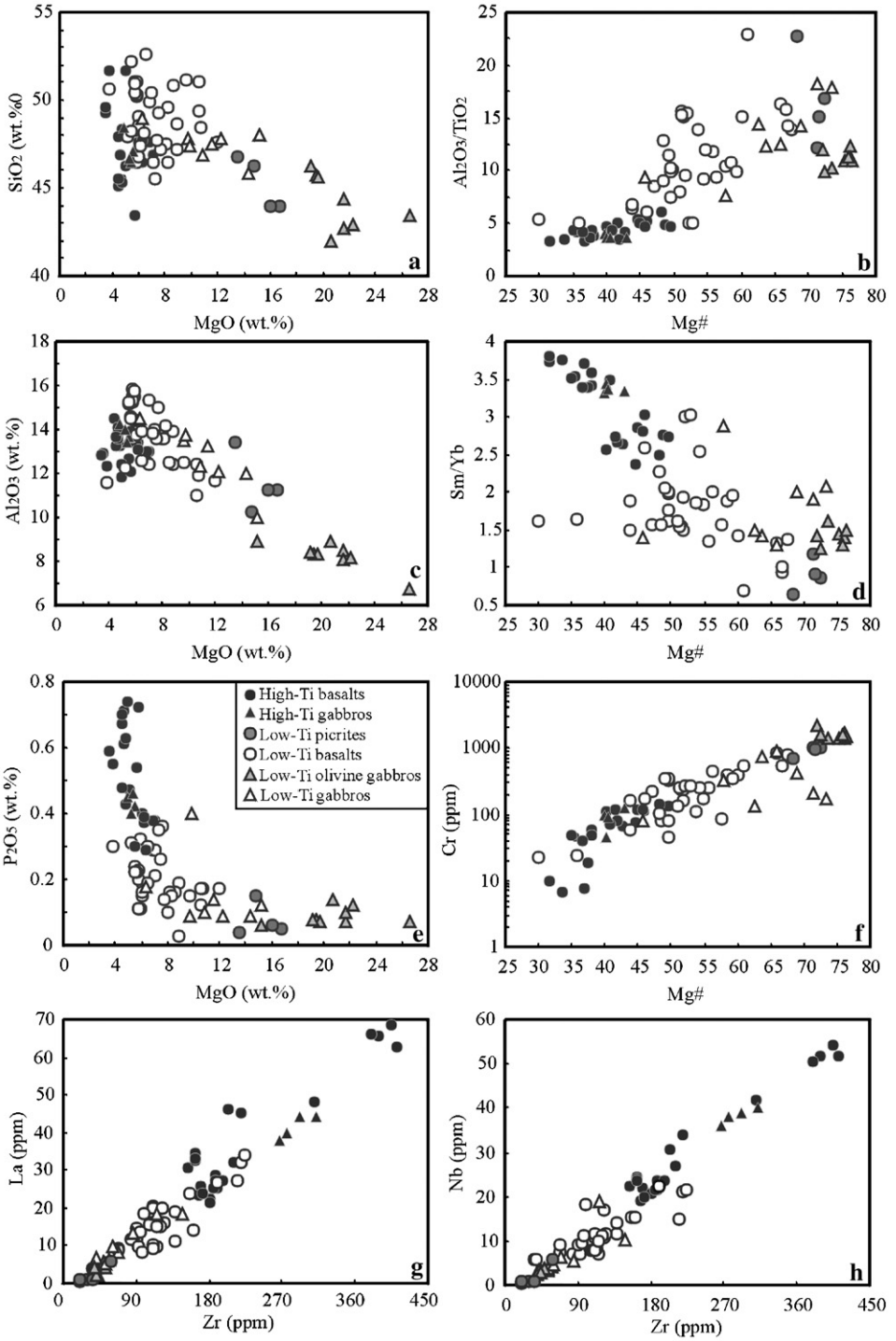

Fig. 3. Variation diagrams of major and trace elements in the flood basalts and mafic intrusions.

of plagioclase (25–60%), clinopyroxene (15–30%), basaltic glass (20–45%), and minor magnetite (<5%). Some olivine-rich basalts also contain minor spinel.

The low-Ti gabbros and olivine gabbros are coarse-grained with granular textures. The olivine gabbros consist of olivine (~10%), clinopyroxene (~50%) and

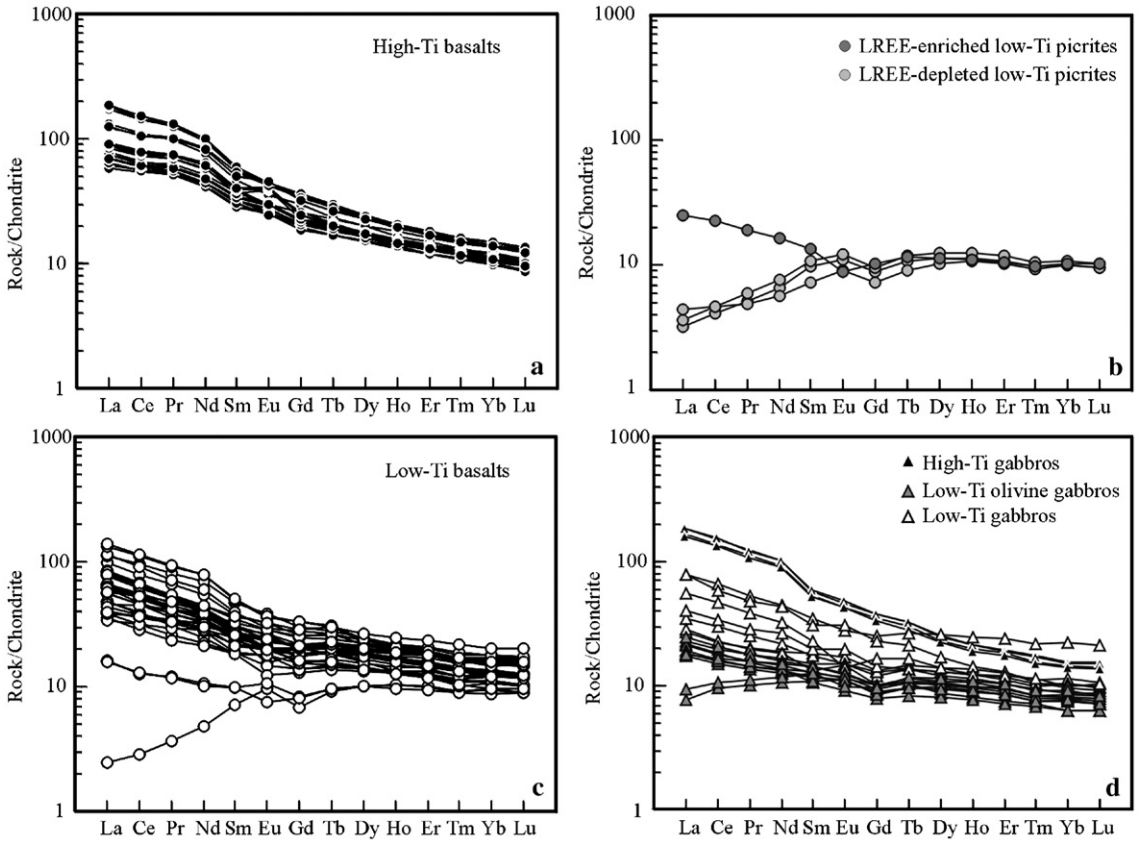

Fig. 4. Chondrite-normalized REE patterns of (a) high-Ti basalts, (b) low-Ti picrites, (c) low-Ti basalts and (d) mafic intrusions. Normalization values are from Sun and McDonough (1989).

plagioclase (~40%). Tabular plagioclase is aligned sub-parallel and partly enclosed by clinopyroxene. The gabbros are composed mostly of clinopyroxene (~45%) and plagioclase (~55%).

4. Analytical methods

4.1. Major and trace element analyses

Sixty-two basalts and 21 gabbros from the Jinping–Song Da district (sampling locations shown in Fig. 1) were analyzed for major and trace elements. Samples were powdered in agate mortars in order to minimize potential contamination. Major elements were determined on fused glass beads using a Philips PW2400 X-ray fluorescence spectrometer at the University of Hong Kong. Trace elements were determined by a VG Plasma-Quad Excell inductively coupled plasma mass spectrometry (ICP-MS) at the University of Hong Kong after a two-day closed-beaker digestion using a mixture of HF and HNO_3 acids in high-pressure bombs (Qi et al., 2000). Pure elemental standard solutions were used for external calibration and AMH-1 (andesite), BHVO-1 (basalt), OH-6 (slate) and GBPG-1 (garnet–biotite plagiogneiss) were used as reference materials. The accuracies of the XRF analyses are estimated to be ±2% (relative) for major elements present in concentrations greater than 0.5 wt.% and ±5% (relative) for minor elements present in concentrations greater than 0.1% (Appendix A). The accuracies of the ICP-MS analyses are estimated to be better than ±10% (relative) for most elements (Appendix B).

4.2. PGE analyses

PGE analyses were carried out using a newly designed Carius tube method (Qi et al., in press). Twelve grams of sample were digested with 30 ml aqua regia in a 75-ml Carius tube, which was placed in a custom-made, high-pressure autoclave. After heating for about 10 h at 300 °C, the solution was cooled and the PGEs were concentrated by Te-coprecipitation. The total procedural blank was lower than 0.003 ppb for Ru, Rh and Ir, 0.020 ppb for Pd, and 0.011 ppb for Pt. The analytical results for two

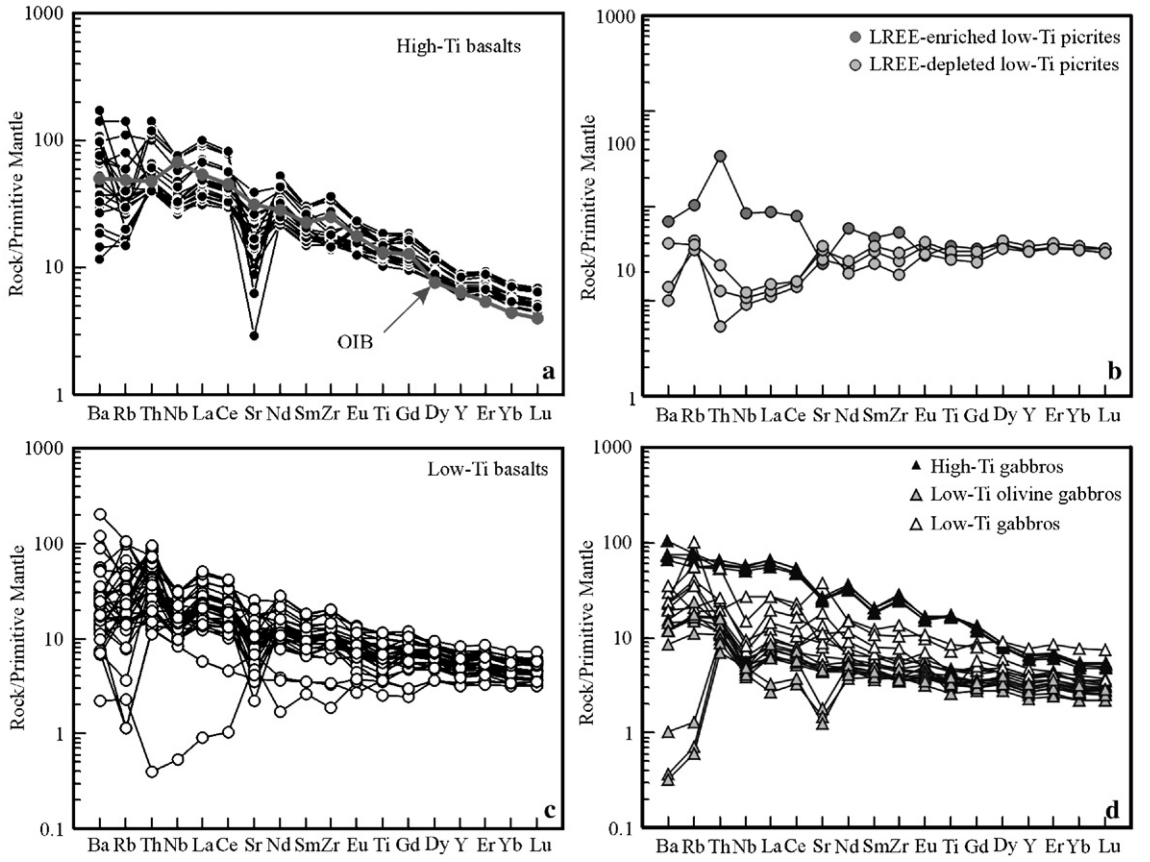

Fig. 5. Primitive mantle-normalized trace element patterns of (a) high-Ti basalts, (b) low-Ti picrites, (c) low-Ti basalts and (d) mafic intrusions. Normalization values are from Sun and McDonough (1989).

reference materials, WGB-1 (gabbro) and TDB-1 (diabase) with low PGE contents, by the new method in this study are in good agreement with the certified and published values for these two standards (Meisel and Moser, 2004; Qi et al., 2004) (Table 3).

4.3. Rb–Sr and Sm–Nd isotopic analyses

Rb–Sr and Sm–Nd isotopic analyses were performed on a VG-354 thermal ionization magnetic sector mass spectrometer at the Institute of Geology and Geophysics, Chinese Academy of Sciences, Beijing. The chemical separation and isotopic measurement procedures are described in Zhang et al. (2001). Procedural blanks were < 100 pg for Sm and Nd and < 500 pg for Rb and Sr. Mass fractionation corrections for Sr and Nd isotopic ratios were based on values of $^{86}Sr/^{88}Sr = 0.1194$ and $^{146}Nd/^{144}Nd = 0.7219$. Uncertainties in Rb/Sr and Sm/Nd ratios are less than ±2% and ±0.5% (relative), respectively. The measured value for Ames Nd was 0.512139±15 (2σ, n=8) and for NBS 987 Sr was 0.710237±25 (2σ, n=8) during the period of data acquisition. The result for Ames Nd is comparable with the published data of 0.512125±10 (Chen et al., 2002). The measured results for USGS standard BCR-1 were Rb 45.49 ppm, Sr 340.0 ppm, $^{87}Sr/^{86}Sr$ 0.704995±25 (2σ) and Sm

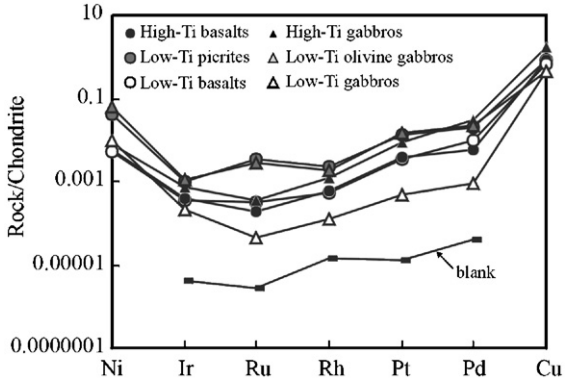

Fig. 6. Chondrite-normalized PGE patterns of (a) high-Ti basalts, (b) low-Ti basalts and (c) mafic intrusions. Average values are used for each group of the rocks. Normalization values are from Anders and Grevesse (1989).

Table 3
PGE compositions of the flood basalts and mafic intrusions in the Jinping–Song Da district

	Ni (ppm)	Ir (ppb)	Ru (ppb)	Rh (ppb)	Pt (ppb)	Pd (ppb)	Cu (ppm)
High-Ti basalts							
HK-14	66.2	0.15	0.07	0.02	0.78	1.66	61.4
HK-38	78.8	0.23	0.18	0.07	7.48	5.71	111
HK-52	65.2	0.29	0.22	0.19	6.05	4.05	144
HK-62	47.5	0.06	0.06	0.03	0.69	1.03	93.6
High-Ti gabbro							
JP-11	85.7	0.34	0.24	0.17	8.41	17.63	225
Picrites							
HK-05	371	0.30	2.05	0.32	13.42	12.21	88.1
HK-41	526	0.66	2.74	0.31	11.70	9.99	125
Low-Ti basalts							
HK-17	229	0.34	1.40	0.11	14.11	16.29	42.3
JP-9	47.9	0.06	0.01	0.01	0.26	0.78	55
HK-49	6.00	0.04	0.04	0.05	0.80	4.14	24.2
HK-98	19.6	0.26	0.07	0.06	0.45	0.44	35.1
JP-4	34.9	0.30	0.02	0.03	0.48	1.02	48.9
JP-6	42.1	0.17	0.09	0.11	7.06	10.61	313
JP-16	83.6	0.18	0.27	0.26	6.93	12.77	204
JP-19	38.4	0.07	0.05	0.01	0.41	0.45	25.8
JP-21-1	16.2	0.04	0.01	0.01	0.41	0.24	7.9
Low-Ti olivine gabbros							
HK-69	643	0.69	2.84	0.21	16.72	14.84	71.8
HK-73	629	0.51	2.08	0.30	14.62	13.39	74.1
HK-81	820	0.44	1.02	0.24	13.40	10.44	18.1
Low-Ti gabbros							
HK-77	22	0.05	0.03	0.01	0.48	0.56	35.1
JP-25	99.5	0.11	0.03	0.01	0.07	0.38	86.7
JP-26	196.2	0.15	0.04	0.02	0.86	0.51	45
Standards							
UMT-1 (this study)		7.34	11.5	8.96	140	111	
UMT-1 (expected)		8.8	10.9	9.5	128	106	
WPR-1 (this study)		15.5	22.8	12.9	297	247	
WPR-1 (expected)		13.5	22	13.4	285	235	
WGB-1 (this study)		0.17	0.13	0.22	6.29	13.2	
WGB-1 (Meisel and Moser, 2004)		0.211	0.144	0.234	6.39	13.9	
WGB-1 (Qi et al., 2004)		0.23	0.16	0.19	5.74	12.0	
TDB-1 (this study)		0.083	0.21	0.49	5.18	23.4	
TDB-1 (Meisel and Moser, 2004)		0.075	0.179	0.471	5.01	24.3	
TDB-1 (Qi et al., 2004)		0.10	0.20	0.35	4.69	20.9	
Blank		0.0025	0.0017	0.0026	0.018	0.037	
Detection limits		0.002	0.002	0.002	0.013	0.022	

6.540 ppm, Nd 28.18 ppm and $^{143}Nd/^{144}Nd$ 0.512634±16 (2σ), which are comparable with the published data of Rb 46.54 ppm, Sr 329.5 ppm, $^{87}Rb/^{86}Sr$ 0.705027±74 (2σ) and Sm 6.676 ppm, Nd 28.77 ppm and $^{143}Nd/^{144}Nd$ 0.512633±35 (2σ) (Chen et al., in press).

5. Analytical results

5.1. Major and trace elements

Both high-Ti series and low-Ti series have distinct chemical compositions. The high-Ti basalts have high total alkalis (Na_2O+K_2O) (Tables 1 and 2) and plot in the alkaline field on the total alkalis–silica (TAS) diagram (Fig. 2). The low-Ti basalts plot in both the alkaline and tholeiitic fields (Fig. 2). The low-Ti picrites also plot in the tholeiitic field on the TAS diagram but are distinguished from the low-Ti basalts by their high MgO (>12 wt.%), low SiO_2 (<47 wt.%) and low total alkalis (<3 wt.%).

Rocks of the high-Ti series have narrow ranges of MgO (3.5 to 7.0 wt.%), and generally have high P_2O_5, La, Nb and Zr and low Cr relative to those of the low-Ti series (Tables 1 and 2, Fig. 3). They have higher Sm/Yb and lower Al_2O_3/TiO_2 ratios than the low-Ti rocks. Rocks of the low-Ti series have up to ~12 wt.% MgO, which generally correlates negatively with P_2O_5, SiO_2 and Al_2O_3 (Tables 1 and 2, Fig. 3a,c,e).

The high-Ti basalts and gabbros are strongly enriched in light REE (LREE) relative to heavy REE (HREE) and display moderately sloping HREE on chondrite-normalized patterns (Fig. 4a and d), with $(Sm/Yb)_N$ ratios of ~3.5 to 3.8. Low-Ti basalts show LREE enrichment patterns (Fig. 4c). All but one of the picrites (HK-5) and one high-Mg basalt (HK-17) are strongly depleted in LREE relative to HREE with $(Ce/Yb)_N$ ratios of 0.3 to 0.5 (Fig. 4b–c). The olivine gabbros are slightly depleted to enriched in LREE with $(Sm/Yb)_N$ ratios of ~1.6 (1.4 to 1.8), whereas the low-Ti gabbros have LREE-enriched patterns with $(Sm/Yb)_N$ ratios of ~2.0 (1.5 to 3.2) (Fig. 4d).

The high-Ti basalts have very negative Sr anomalies and slightly negative Nb and Ti anomalies on primitive

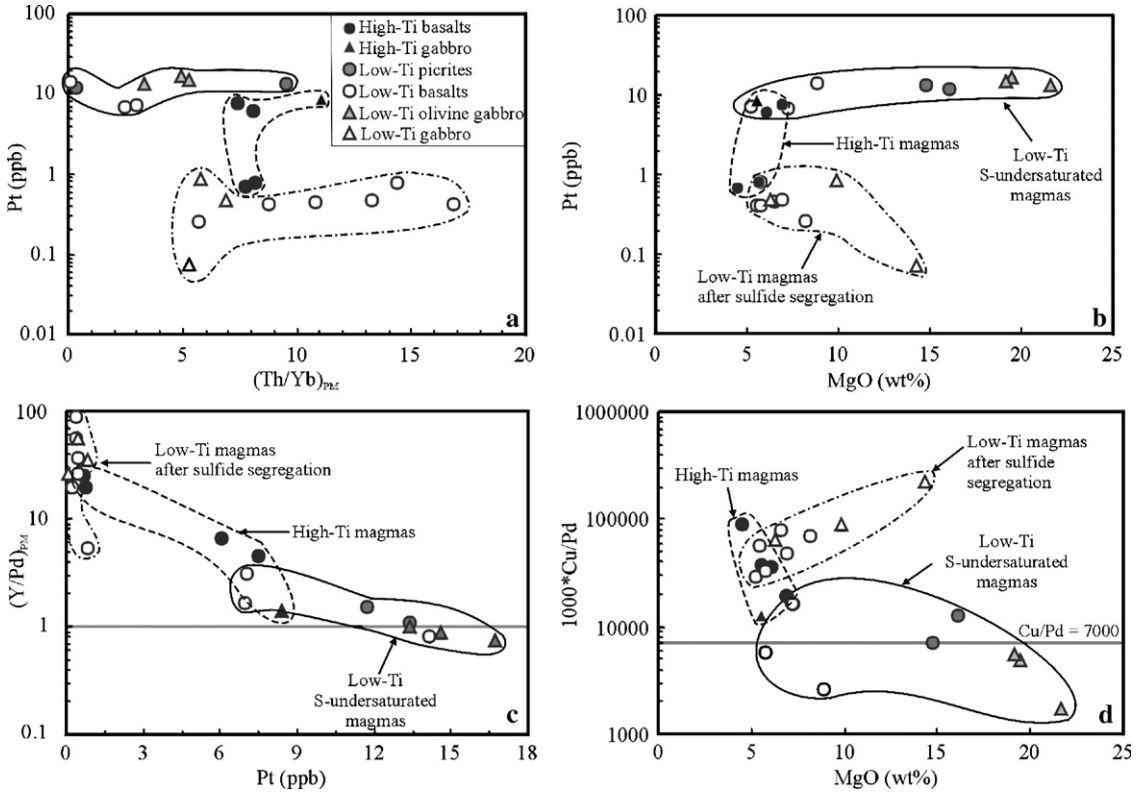

Fig. 7. Variation diagrams of Pt versus $(Th/Yb)_{PM}$ (a), Pt and Pd versus MgO (b), $(Y/Pd)_{PM}$ versus Pt (c) and Cu/Pd versus MgO (d) in the flood basalts and mafic intrusions. Primitive mantle values are from Sun and McDonough (1989); Cu/Pd = 7000 is the ratio of primitive mantle (after Barnes and Maier, 1999).

mantle-normalized trace element patterns (Fig. 5a). The high-Ti gabbros have patterns similar to the high-Ti basalts (Fig. 5d). Low-Ti basalts have smaller negative Sr anomalies and larger negative Nb and Ti anomalies than those for the high-Ti basalts (Fig. 5c). The LREE-depleted picrites and high-Mg basalt show positive Sr anomalies and pronounced Th depletion, whereas the LREE-enriched picrites show negative Sr anomalies and positive Th anomalies (Fig. 5b–c). The low-Ti gabbros show patterns similar to those of the low-Ti basalts, but have both positive and negative Sr anomalies (Fig. 5d).

5.2. Platinum-group elements

All rocks exhibit similar chondrite-normalized chalcophile elemental patterns enriched in Ni and Cu but depleted in Ir and Ru (Fig. 6, Table 3). However, picrites and low-Ti olivine gabbros with relatively high PGE contents show slightly negative Ir and Rh anomalies and positive Ru anomalies (Fig. 6). Low-Ti basalts display two distinct patterns; one type with low Th/Yb ratios and high Pt and Pd abundances and the other with high Th/Yb ratios and low Pt and Pd abundances (Fig. 7a). The low-Ti plutons also fall into two distinct groups; low-Ti olivine gabbros with high MgO, Pt and Pd abundances, whereas low-Ti gabbros with low MgO, Pt and Pd abundances (Fig. 7b). The picrites, low-Ti basalts with low Th/Yb ratios, and olivine gabbros have Y/Pd and Cu/Pd ratios lower than the low-Ti basalts with high Th/Yb ratios and the low-Ti gabbros (Fig. 7c–d).

5.3. Sm–Nd and Rb–Sr isotopic compositions

The basalts in this region have isotopic compositions similar to lavas elsewhere in the ELIP but are characterized by a wider range of $\varepsilon Nd(t)$ values and initial $(^{87}Sr/^{86}Sr)_i$ ratios (Table 4 and Fig. 8). The analyzed samples fall near the "mantle array" but have distinctly high Sr ratios (Fig. 8), indicating some modification of Sr isotopes by hydrothermal alteration. The high-Ti series shows a limited range of $\varepsilon Nd(t)$ values (+0.5 to +1.1) and initial $^{87}Sr/^{86}Sr$ ratios (0.705 to 0.706). One picrite has the highest $\varepsilon Nd(t)$ value (+7.0) and lowest initial $^{87}Sr/^{86}Sr$ ratio (0.704), indicating formation from a depleted mantle source, whereas the other picrite has a very negative $\varepsilon Nd(t)$ value (−7.8) and

Table 4
Sm–Nd and Rb–Sr isotopic compositions of the flood basalts and mafic intrusions in the Jinping–Song Da district

Samples	Rb	Sr	$^{87}Rb/^{86}Sr$	$^{87}Sr/^{86}Sr+2\sigma$	$(^{87}Sr/^{86}Sr)_i$	Sm	Nd	$^{147}Sm/^{144}Nd$	$^{143}Nd/^{144}Nd+2\sigma$	$(^{143}Nd/^{144}Nd)_i$	$\varepsilon Nd(t)$
High-Ti basalts											
HK-14	26.4	219	0.3468	0.706614±12	0.7053	8.52	38.4	0.1343	0.512571±11	0.5123	+0.8
HK-38	26.3	364	0.2217	0.706669±13	0.7058	7.23	29.8	0.1468	0.512578±9	0.5123	+0.5
HK-52	11.6	359	0.0933	0.706331±9	0.7060	7.16	31.6	0.1373	0.512593±13	0.5124	+1.1
HK-62	12.2	515	0.0681	0.705514±12	0.7053	8.15	39.4	0.1252	0.512554±11	0.5123	+0.7
High-Ti gabbro											
JP-11	48.2	560	0.2489	0.706561±19	0.7056	8.86	43.5	0.1230	0.512538±13	0.5123	+0.5
Picrites											
HK-05	6.62	63.9	0.2974	0.714255±14	0.7132	2.39	8.81	0.1639	0.512182±17	0.5119	−7.8
HK-41	2.25	102	0.0636	0.704362±14	0.7041	2.07	4.40	0.2854	0.513146±13	0.5127	+7.0
Low-Ti basalts											
HK-17	1.34	107	0.0362	0.705549±15	0.7054	1.20	2.42	0.3011	0.513143±22	0.5126	+6.4
HK-49	27.4	133	0.5957	0.714976±13	0.7128	4.87	20.6	0.1434	0.512023±11	0.5118	−10.2
HK-98	2.47	419	0.0169	0.708546±14	0.7085	3.77	16.3	0.1404	0.512018±8	0.5118	−10.2
HK-98[a]	2.13	408	0.0152	0.708525±13	0.7085	3.67	16.0	0.1386	0.512021±12	0.5118	−10.1
JP-4	29.8	286	0.3016	0.707572±20	0.7065	8.21	36.4	0.1364	0.512399±12	0.5122	−2.7
JP-6	12.7	222	0.1647	0.705555±23	0.7049	5.98	21.1	0.1715	0.512760±15	0.5125	+3.2
JP-9	12.3	88	0.4034	0.707658±20	0.7062	3.54	13.8	0.1556	0.512521±11	0.5123	−0.9
JP-16	31.2	232	0.3888	0.706220±19	0.7048	4.00	13.2	0.1838	0.512890±20	0.5126	+5.3
JP-19	22.4	327	0.1982	0.708348±18	0.7076	6.12	26.5	0.1395	0.512232±14	0.5120	−6.0
JP-21-1	11.2	93.8	0.3468	0.708788±20	0.7075	4.68	18.7	0.1512	0.512344±10	0.5121	−4.2
Low-Ti olivine gabbros											
HK-69	15.4	150	0.2952	0.709801±13	0.7087	2.19	7.50	0.1766	0.512443±10	0.5121	−3.1
HK-73	10.1	126	0.2312	0.708168±14	0.7073	2.31	7.99	0.1746	0.512386±12	0.5121	−4.2
HK-81	0.35	30.6	0.0332	0.708806±14	0.7087	1.58	4.49	0.2124	0.512679±8	0.5123	+0.3
Low-Ti gabbros											
HK-77	33.3	152	0.6310	0.714534±14	0.7122	4.81	18.7	0.1553	0.512189±9	0.5119	−7.4
JP-25	23.2	293	0.2292	0.707539±16	0.7067	2.07	8.13	0.1542	0.512412±8	0.5121	−3.0
JP-26	14.0	831	0.0487	0.706353±20	0.7062	4.79	19.4	0.1492	0.512764±8	0.5125	+4.0

Note: λ (^{87}Rb)=1.42×10^{-11} y^{-1}, λ (^{147}Sm)=6.54×10^{-12} y^{-1}. εNd values were calculated relative to present-day chondrite values of $^{143}Nd/^{144}Nd$=0.512638, $^{147}Sm/^{144}Nd$=0.1967, $^{87}Sr/^{86}Sr$=0.7045 and $^{87}Rb/^{86}Sr$=0.0827. Initial ratios were calculated assuming age of 260 Ma.
[a] This is a duplicate analysis for sample HK-98.

the highest initial $^{87}Sr/^{86}Sr$ ratio (0.713) of all the rocks. The low-Ti basalts have εNd(t) values ranging from +6.4 to −10.2 and $(^{87}Sr/^{86}Sr)_i$ ratios from 0.705 to 0.713, similar to those of the low-Ti gabbros, which have εNd(t) values ranging from +4.0 to −7.4 and $(^{87}Sr/^{86}Sr)_i$ ratios from 0.706 to 0.712. In general, the $(^{87}Sr/^{86}Sr)_i$ ratios of the low-Ti series correlate negatively with the εNd(t) values and show a trend from the picrites toward enriched mantle II (EMII) (Fig. 8).

6. Discussion

6.1. Effects of alteration

The Emeishan flood basalts and associated mafic–ultramafic intrusions have been variably metamorphosed and altered following their eruption and burial. Alteration may have significantly changed the concentrations of many mobile elements, such as Cs, Rb, Ba, K and Sr, which scatter broadly and incoherently when plotted on variation diagrams. The flattening of some of the chondrite-normalized patterns from Pt to Pd (Fig. 6) could be an artifact of alteration (Ely and Neal, 2003), because Pd can be preferentially mobilized relative to the other PGEs by hydrothermal alteration (Barnes et al., 1985).

However, both REE and high field strength elements (HFSE, such as Nb, Ta and Ti) remain immobile during metamorphism or hydrothermal alteration (e.g., Staudigel and Hart, 1983) because they have high valences and electronegativities, small radii, and strong chemical bonds in both primary and secondary minerals. Thus,

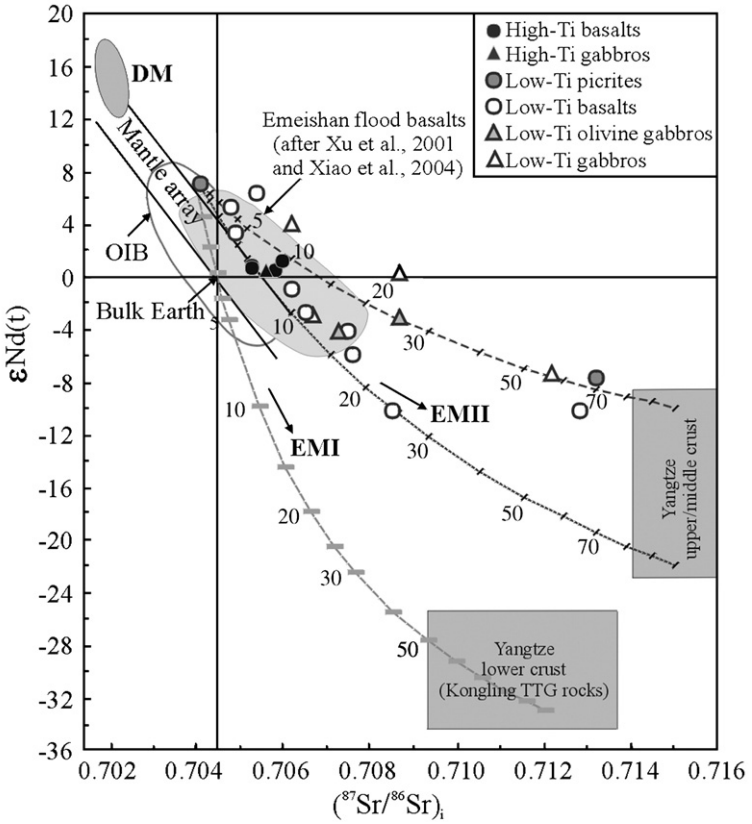

Fig. 8. εNd(*t*) (*t*=260 Ma) values versus initial $^{87}Sr/^{86}Sr$ diagram for the flood basalts and mafic intrusions. DM (depleted mantle), mantle array and EMI and EMII trends are after Zindler and Hart (1986). Bulk Earth data from Depaolo (1988). OIB data are from Wilson (1989). The Yangtze upper/middle crust and lower crust data are from Gao et al. (1999), Ma et al. (2000), and Chen and Jahn (1998). The numbers indicate the percentages of participation of the crustal materials. The calculated parameters of Nd (ppm), εNd(*t*), Sr (ppm) and $(^{87}Sr/^{86}Sr)_i$ are 4.4, +7, 102 and 0.704 from picrites in northern Vietnam as parental magmas; 20, −22, 220, 0.715 and 20, −10, 220, 0.715 as two components of the Yangtze middle/upper crust.

the ratios between these elements remain constant. Good linear correlations between La and other REE and HFSEs, indicate that the REE and HFSEs are immobile during the greenschist metamorphism and hydrothermal alteration that affected the rocks (e.g., Fig. 3f–h). Therefore, we conclude that the εNd(*t*) values and the concentrations of PGEs, HFSE, REEs, Th, Cr and Al reported in this study are primary and can be used to examine the petrogenesis.

6.2. Nature of mantle sources and parental magmas

The generation of continental flood basalts has been debated on the nature and relative contribution of the asthenospheric and lithospheric mantle. Although most agreed a deeper asthenospheric mantle plume source for the high-Ti basalts (e.g., Lightfoot et al., 1993), many workers attributed the large variation in the composition of the low-Ti basalts to a metasomatized sub-continental lithospheric mantle (e.g., Hergt et al., 1989; Lightfoot et al., 1993; Späth et al., 2001; Larsen et al., 2003). However, the lithospheric mantle was not considered to give rise to magmas with diverse chemical characteristics because it is the coldest part of the mantle, which melts only if its solidus is depressed by the presence of volatiles (Arndt et al., 1998; Kieffer et al., 2004). The geochemical signatures of the low-Ti series in this study support its derivation from a depleted mantle source with substantially crustal contamination.

6.2.1. High-Ti basalts

The high-Ti basalts in the Jinping–Song Da district display trace element patterns similar to OIB (Fig. 5a). Their εNd(*t*) values varying from +0.5 to +1.1 are also typical of an OIB mantle source (Fig. 8), suggesting derivation from the same plume source as the high-Ti flood basalts elsewhere in the ELIP (e.g., Xu et al., 2001; Xiao et al., 2004).

The obviously negative Sr anomalies of the high-Ti basalts may have been related to extensive fractionation of plagioclase from high-Ti magmas. Their moderately sloping chondrite-normalized HREE patterns (Fig. 4a) and relatively high $(Gd/Yb)_{PM}$ ratios (1.7 to 2.6) indicate the presence of residual garnet during partial melting because garnet has high partition coefficients for HREE (e.g., Jenner et al., 1990; Green, 1994). In addition, these lavas have relatively high Tb/Yb ratios, which generally increase with increasing Sm (Fig. 9b). Such high Tb/Yb ratios also suggest garnet in the partial melting residue, a feature of melting at greater depths.

Ytterbium is compatible with garnet but not with clinopyroxene, thus the plot of Sm versus Sm/Yb diagram can be used to model the source characteristics in terms of mineralogy (Aldanmaz et al., 2000) (Fig. 9d). Partial melts from a spinel-lherzolite source have Sm/Yb ratios similar to that of the mantle and thus form a horizontal melting trend that lies within, or close to, a mantle array defined by depleted-MORB mantle (DMM) and primitive mantle (PM) compositions, whereas partial melts from a garnet-lherzolite source (with garnet residue) will have significantly higher Sm/Yb ratios than the mantle source (Aldanmaz et al., 2000). The rocks of the high-Ti series are displaced from the mantle array (= spinel-lherzolite melting trend) to higher Sm/Yb ratios and plot between the melting trajectories for garnet- and garnet+spinel-lherzolite, indicating that the high-Ti series was derived from a garnet+spinel-bearing mantle with more garnet than spinel, suggesting the formation at a depth of approximately 200 to 400 km (after Wyllie, 1981).

The degree of partial melting to form the high-Ti basalts is constrained by the high concentrations of incompatible elements of the rocks. The relatively low Al_2O_3/TiO_2 ratios (~4 compared with ~20 in primitive mantle) and high $(Sm/Yb)_{PM}$ ratios (2.6 to 4.2) (Fig. 9c) of the high-Ti basalts indicate small degrees of partial melting of a relatively deep mantle source. The degree of partial melting was probably less than ~8% for the parental magmas of the high-Ti basalts on the basis of Sm versus Sm/Yb ratios (Fig. 9d). The variable Sm/Nd ratios and constant $\varepsilon Nd(t)$ values of the high-Ti basalts are consistent with a fractional crystallization (FC) trend (Fig. 10a).

6.2.2. Low-Ti series

6.2.2.1. LREE-depleted picrites. Although the LREE-depleted picrites in northern Vietnam were described as komatiites by Hanski et al. (2004), they do not have typical spenifix texture. The picrites with high positive $\varepsilon Nd(t)$ values (+7) and low $(Ce/Yb)_N$ ratios (0.3 to 0.5) indicate a long-term depletion of the mantle source in LREE, which is similar to N-MORB but exceptional in LIPs (e.g., Carlson, 1991). In general, rocks having the greatest degree of depletion are found among the most primitive lavas. Examples include picrites from the North Atlantic Igneous Province (Saunders et al., 1997) and Horingbaai intrusions in the coastal region of Namibia (Thompson and Gibson, 2000). Therefore, the picrites in the Song Da region may belong to the rare examples of LIP-related magmas retaining clear evidence for a strongly chemical and isotopic depleted mantle source (Hanski et al., 2004).

The compositions of the picrites provide tight constraints on the conditions of melting and compositions of mantle sources. The picritic liquids had an Mg# of ~90 based on olivine compositions with high Ni (~1000 ppm) and Cr (~2000 ppm) contents (Hanski et al., 2004). The concentrations of some incompatible trace elements of the picrites are very low. For example, Ta concentrations are only 1.5–10 times the primitive mantle value. The picrites have remarkably high Al_2O_3/TiO_2 ratios (~17) (Fig. 9c) and highly depleted LREE relative to HREE with $(Sm/Yb)_N$ ratios of 0.7 to 1.3 and $(Tb/Yb)_N$ ratios of 0.9 to 1.1. The high concentrations of MgO, Ni and Cr in the picrites suggest that the source contained olivine and had a dominantly peridotitic, rather than pyroxenitic or eclogitic (Arndt et al., 1998). The picrites have compositions similar to those of meymechites in Siberia, which are presumed to have been produced by near-solidus melting of dry mantle peridotite at very high pressures (8–10 GPa), corresponding to a depth of 250–300 km (Arndt et al., 1998). Picrites in Song Da were also thought to have formed from a dry parental magma with extremely low water contents (<0.03 wt.%) (Hanski et al., 2004). However, they contain incompatible trace elements much lower than the meymechites in Siberia. On the basis of the equations of Herzberg and Zhang (1996), the high Al_2O_3 (~11.5 wt.%) and MgO (15 wt.%) contents and high Al_2O_3/TiO_2 ratios (16.7) of the picrites correspond to high-degree partial melting of dry mantle peridotite at pressures of 2.8–3.8 GPa (corresponding to a depth of 100–120 km). The degree of partial melting was probably ~20% for the picritic magmas on the basis of Sm versus Sm/Yb ratios of the rocks (Fig. 9d). Therefore, the picritic magma could have formed by high-temperature anhydrous melting at relatively shallow levels in the upper mantle.

6.2.2.2. LREE-enriched picrites. One LREE-enriched picrite has a very negative $\varepsilon Nd(t)$ value (<−7), and high

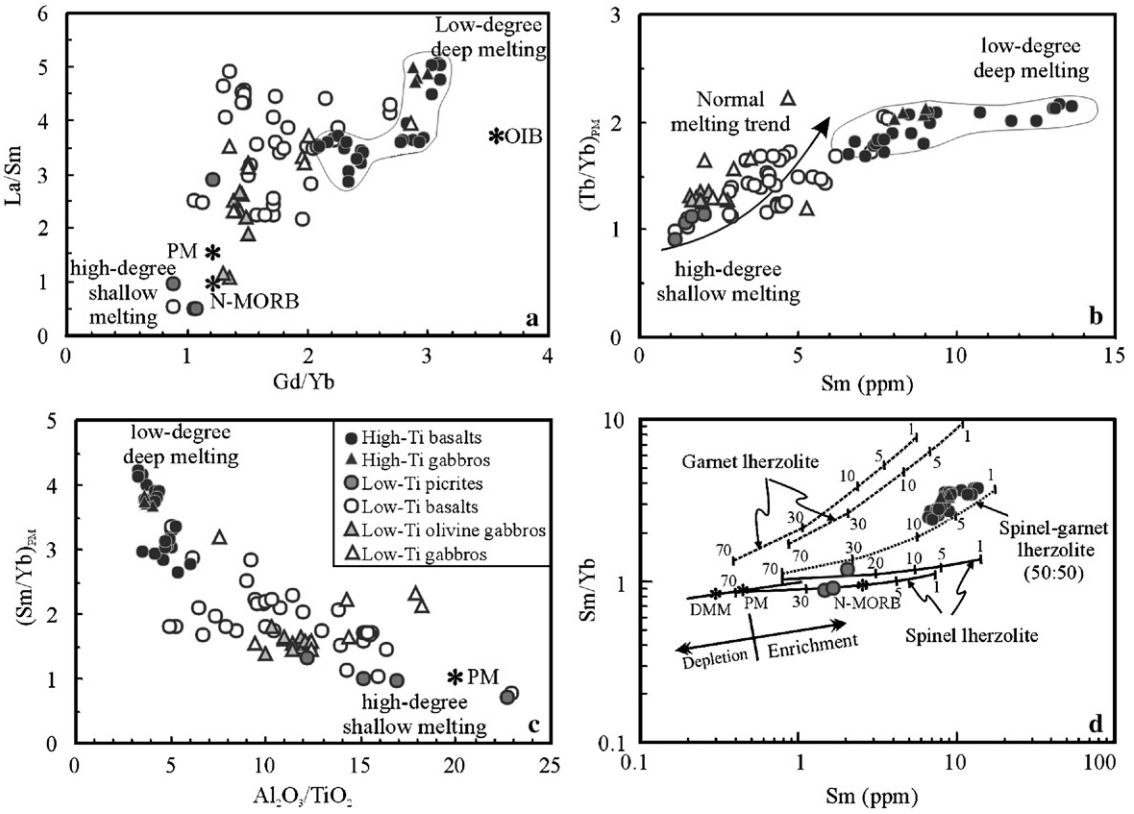

Fig. 9. Plots of elemental ratios of the flood basalts and mafic intrusions showing the nature and origin of the parental magmas and mantle process (a–c) and plots of Sm versus Sm/Yb showing melt curves (d), the referred melt curves are after Aldanmaz et al. (2000) and references therein. Primitive mantle (PM) and N-MORB compositions are from Sun and McDonough (1989).

($^{87}Sr/^{86}Sr)_i$ ratio (>0.712) (Fig. 8), Th, Zr and LREE (Table 1). This feature cannot be explained by crustal contamination of the parental picritic magmas, because in this case high degrees of crustal contamination (~50%) are required (Fig. 8). Such high degrees are impossible and would have severely modified the major element composition of the magmas. For example, SiO_2 contents would have been significantly increased such that the rocks should contain much higher SiO_2 than the picrite (Table 1). In contrast, preferential leaching of volatiles and more mobile large-ion lithophile elements (LILE), such as Rb, Sr, Ba and U, from subducted slab may fractionate them from less mobile elements such as Th, Nb, Ta and LREE, resulting in the observed geochemical signatures (Fig. 5b). Thus, our favored interpretation is that the LILE-enriched geochemical signature of the picrite was generated by interaction between depleted asthenospheric melts and metasomatized lithospheric mantle, which may have been modified by previous subduction. Previous subduction in this region was likely related to subduction of the Lancangjiang–Changning–Menglian ocean during the Devonian–Carboniferous and the subduction of the Jinshajiang–Ailaoshan–Song Ma back-arc basin which was initiated in the early Permian (Wang et al., 2000). However, such modification of the depleted mantle source is assumed to have occurred locally as only a few samples show such LILE-enriched geochemical signatures.

6.2.2.3. Low-Ti basalts. Most of the low-Ti basalts have low MgO (5–7.6 wt.%) and Mg# (<55) and high SiO_2, generally highly evolved relative to the picrites, although a few have higher MgO and lower SiO_2. The least-contaminated low-Ti basalts and the picrites have similar chondrite-normalized REE and trace element patterns (Fig. 5b–c), Sm/Nd and Th/Yb ratios, and $\varepsilon Nd(t)$ values (Figs. 8 and 10a). These similarities suggest that the low-Ti tholeiitic magmas may have formed from picritic parental magmas and probably experienced fractionation of olivine and clinopyroxene (±plagioclase) because they are the dominant phenocrysts of the picrites.

6.3. Crustal contamination

Relatively high $(Nb/La)_{PM}$ ratios (~0.8), low $(Th/Nb)_{PM}$ ratios (~1.4) and slightly negative Nb (Ta) anomalies of the high-Ti basalts indicate that crustal contamination was not significant (Fig. 10b).

On a plot of εNd(*t*) versus $^{147}Sm/^{144}Nd$ (Fig. 10a), the low-Ti basalts with positive εNd(*t*) values define a horizontal trend produced by a combination of partial melting and fractional crystallization, whereas the others with negative εNd(*t*) values define an inclined trend, which reflects binary mixing between a mantle source component and the continental crust, as indicated by high $(Th/Nb)_{PM}$ ratios of the rocks (Fig. 10b). On the εNd(*t*) versus $(^{87}Sr/^{86}Sr)_i$ diagram (Fig. 8), the low-Ti lavas follow a bulk mixing trend between a picritic melt, as represented by the most depleted picrite in this region, and the Yangtze upper/middle crust with a maximum of ~25% contamination. Therefore, the low-Ti basalts were probably derived from primary picritic magmas that underwent crystal fractionation and acquired their

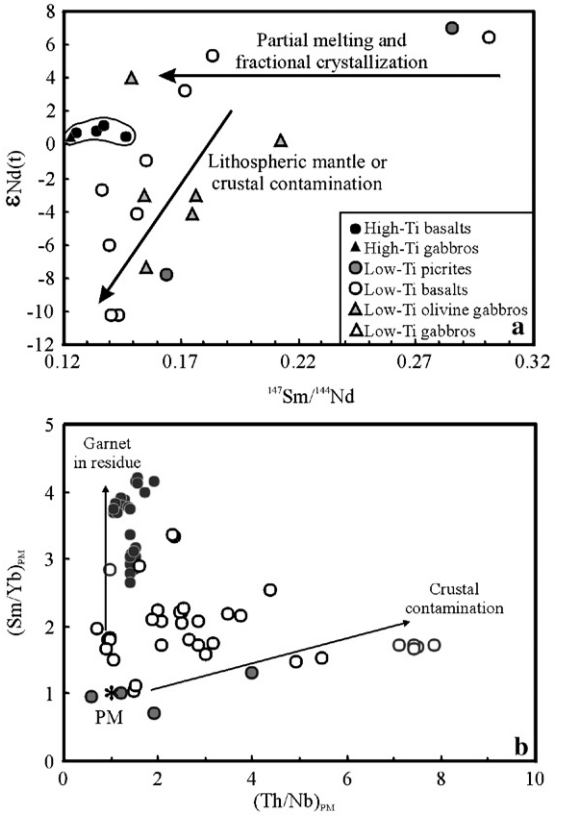

Fig. 10. $^{147}Sm/^{144}Nd$ versus εNd(*t*) values (a) and $(Th/Nb)_{PM}$ versus $(Sm/Yb)_{PM}$ ratios (b) in the flood basalts and mafic intrusion. Primitive mantle values are from Sun and McDonough (1989).

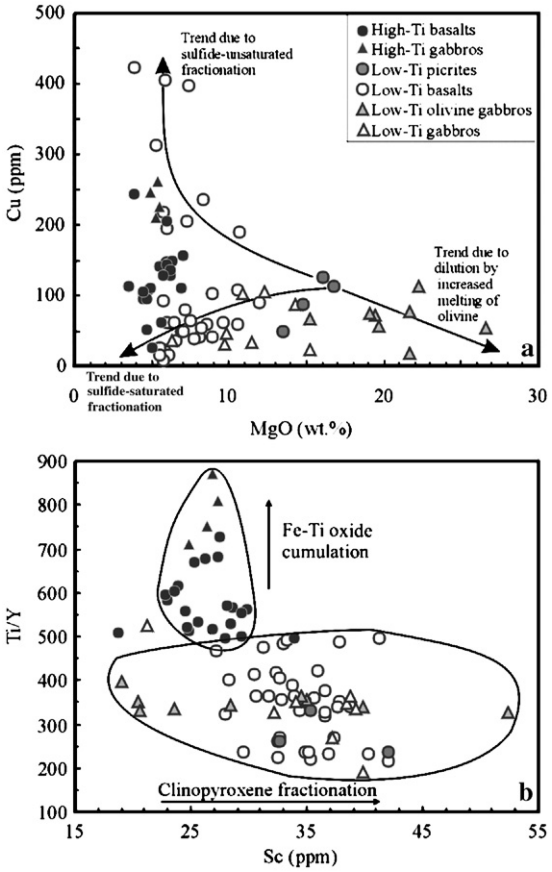

Fig. 11. MgO versus Cu (a) and Sc versus Ti/Y (b) of the flood basalts and mafic intrusions showing the genetic relationship of the flood basalts and mafic intrusions.

significant crustal signature through interaction with country rocks (cf., Arndt and Christensen, 1992; Wooden et al., 1993; Griselin and Arndt, 1996). This model is consistent with the crude correlation between trace element ratios and εNd(*t*) values of the low-Ti lavas (Fig. 10a) and the highly evolved nature of the low-Ti basalts.

6.4. Sulfide segregation

The diversity of the ELIP rocks in the Jinping–Song Da district may have resulted from distinct mantle sources, different fractional crystallization processes and variable degrees of crustal contamination. These processes resulted in variable sulfide segregation in different rocks.

6.4.1. No sulfide segregation in the high-Ti series

The high-Ti series defines a trend of increasing Cu with nearly constant MgO (Fig. 11a). The very low Ni/

Cu ratios (<1) are consistent with crystallization of olivine and, to a lesser extent, orthopyroxene which remove Ni from magmas and leave Pd, Pt and Cu in the residual magma under S-undersaturated conditions (Keays, 1995; Naldrett, 2004). The high and variable Ti/Y ratios (490 to 871) of the high-Ti series with constant Sc contents are indicative of Fe–Ti oxide accumulation (Fig. 11b), consistent with abundant magnetite and ilmenite in these rocks. This is also supported by the low $(Ni/Ir)_{PM}$ ratios of ~0.7 (from 0.4 to 1.4). Because PGEs partition strongly into sulfide liquids, the removal of sulfide by equilibrium fractionation will deplete the magmas in PGEs, such that the Cu/Pd and Ni/Ir ratios of the magmas rise dramatically (Barnes and Maier, 1999). Thus, the low $(Ni/Ir)_{PM}$ ratios indicate removal of olivine/orthopyroxene from S-undersaturated magmas rather than the removal of sulfide from S-oversaturation magmas. This suggests that the evolution of the high-Ti series was controlled by silicate fractionation rather than sulfide saturation.

Rocks of the high-Ti series have Cu/Pd ratios ~5.6 (1.8 to 13) times the primitive mantle and low Cu/Zr ratios (0.13 to 1.07) relative to the picrites (Cu/Zr>1). Because of higher partition coefficient of PGE into sulfide than Cu, the high Cu/Pd ratios and low Cu/Zr ratios are consistent with sulfide fractionation: either in the mantle or during the evolution of the magmas. The relatively constant PGE contents of the high-Ti rocks do not support S-saturated differentiation in the magma, because such differentiation would have resulted in highly variable PGE contents of the rocks. It has been suggested that the low degrees of partial melting produce S-saturated magmas and leave behind sulfide melts in the mantle (Keays, 1995). Thus, relatively constant but poor PGE contents of the high-Ti rocks are supportive of low degrees of partial melting.

6.4.2. Variable sulfide segregation of the low-Ti series

S-undersaturated basaltic magmas usually have $(Y/Pd)_{PM}$ ratios close to 1 due to similar incompatibilities of two elements, but segregation of a sulfide melt will be accompanied by large depletions of Pt and Pd relative to Y in the remaining silicate melt (Brügmann et al., 1993). Thus, Y/Pd ratios are useful indicators of sulfide saturation in magmas. The picrites have $(Y/Pd)_{PM}$ ratios close to 1 (1.1 to 1.5), relatively high MgO and low Cu contents (Fig. 11a), and Cu/Zr>1, indicating that the picritic magmas were S-undersaturated, which have been produced by large degrees of partial melting of a S-undersaturated upper mantle source (Keays, 1995).

The low-Ti basalts display either S-undersaturated or S-oversaturated trend on the Cu versus MgO plot (Fig. 11a) (cf., Andersen et al., 2002). The one with a S-undersaturated trend shows a dramatic increase in Cu with decreasing of MgO. The other with a S-oversaturated trend shows a decrease Cu with decreasing of MgO. On the same diagram, the low-Ti olivine gabbros show a decrease of Cu with increasing of MgO, indicating the formation from S-undersaturated magmas by high-degree partial melting (>20–25%, Barnes and Picard, 1993), whereas the low-Ti gabbros show a similar S-oversaturated trend to that for the low-Ti basalts.

The low-Ti basalts with a S-undersaturated trend are characterized by positive $\varepsilon Nd(t)$ values (+3.2 to +5.3), relatively high Pt and Pd contents and Cu/Zr ratios of >1. They also have low $(Y/Pd)_{PM}$ (0.8 to 3.0) (Fig. 7c), Th/Yb (~0.6), and $(Cu/Pd)_{PM}$ ratios (0.2 to ~3) (Fig. 7d). The positive $\varepsilon Nd(t)$ values and low Th/Yb ratios of these basalts indicate minor crustal contamination, whereas their high Cu/Zr and low Y/Pd and Cu/Pd ratios indicate S-undersaturation of the magmas (cf., Keays, 1995; Kerr, 2003). The olivine gabbros have compositions similar to those of the PGE-rich, low-Ti basalts. The trend of decreasing Cu with increasing MgO of the olivine gabbros indicates that the Cu contents of the magmas were diluted by increasing degrees of partial melting largely involving olivine, and the magmas were thus S-undersaturated.

The low-Ti basalts and gabbros with a S-oversaturated trend (Fig. 11a) have identical compositions and are characterized by high $(Y/Pd)_{PM}$ (5.4 to 86.8) and low Cu/Zr ratios (<1) and low Pt and Pd contents. The low Cu/Zr ratios generally resulted from the removal of sulfide which affects Cu, but not Zr (e.g., Lightfoot et al., 1994; Kerr, 2003). The very negative $\varepsilon Nd(t)$ values (−0.9 to −10.2) and relatively high Th/Yb ratios (~2) of the low-Ti basalts are indicative of extensive crustal contamination. Their high Cu/Pd ratios (Fig. 7d) likely reflect segregation of large amounts of sulfide somewhere at depth prior to the eruption.

Economically important Ni–Cu–(PGE) sulfide mineralization could have formed when the low-Ti magmas with high degrees of crustal contamination reached S-oversaturation and produced immiscible sulfide melts. Emplacement of the magmas containing the sulfide melts probably formed the mafic–ultramafic intrusions hosting Ni–Cu–(PGE) sulfide deposits, such as the Baimazhai and Ban Phuc intrusions in this region (Glotov et al., 2001; Wang and Zhou, 2006). On the other hand, the residual melts after sulfide segregation would have been depleted in PGE and would have intruded elsewhere to form PGE-depleted, low-Ti gabbroic bodies or

have been erupted to form the low-Ti basaltic lavas. A similar relationship has also been recognized in the Siberian Traps (Lightfoot and Keays, 2005), the Coppermine River flood basalts and the Keweenawan Oslar volcanic Group in Canada (Lightfoot et al., 1991). In Siberia, there is a clear spatial and genetic link between Ni-, Cu- and PGE-depleted flood basalts and the ore deposits (Lightfoot and Keays, 2005), and the lavas with the lowest Ni and Cu concentrations show the most extensive crustal contamination (Lightfoot and Hawkesworth, 1997).

6.5. An integrated model

We propose that the Emeishan mantle plume gave rise to magmas with distinct compositions. The high-Ti magmas probably formed first at depths of ~200 to 400 km during initial upwelling by low degrees of partial melting of enriched mantle material. The high-Ti magmas were probably volatile-rich, as evidenced by the presence of primary biotite in these rocks (Xu et al., 2001). The relatively light and volatile-rich high-Ti magmas could have ascended rapidly to the surface, such that they escaped crustal contamination. In contrast, the low-Ti and LREE-depleted picritic magmas were produced later at shallower depths (100–120 km) by high degrees of partial melting of a warm, depleted mantle source. The depleted mantle source may have been locally modified by subducted oceanic crust so as to generate an enriched mantle source from which minor LREE-enriched picrites formed. This scenario envisages the presence of two very different, coeval plumbing systems during the evolution of the ELIP. The low-Ti basalts may have evolved from the picritic parental magmas by an AFC process, and extensive crustal contamination was the major control on S-oversaturation and sulfide segregation in some of the low-Ti basaltic magmas. The heterogeneous compositions of these rocks may reflect an absence of steady state conditions in the crustal magma chambers or that the residual magmas were not in equilibrium with the crystallized phases, such as olivine, clinopyroxene and plagioclase (cf., Wooden et al., 1993).

Thus, our model accounts for the several kinds of mafic–ultramafic intrusions in the ELIP: (1) high-Ti gabbroic intrusions equivalent to the high-Ti basalts, which are unrelated to sulfide mineralization; (2) low-Ti PGE-rich olivine gabbroic intrusions, equivalent to the PGE-enriched low-Ti basalts in composition, which formed from S-undersaturated magmas; (3) low-Ti PGE-depleted gabbroic intrusions, equivalent to PGE-depleted low-Ti basalts, which formed from magmas that underwent sulfide saturation due to extensive crustal contamination; and (4) low-Ti mafic–ultramafic intrusions hosting Ni–Cu–(PGE) sulfide deposits.

7. Conclusions

High-Ti and low-Ti series of the ~260-Ma ELIP in the Jinping–Song Da district show distinctly geochemical characteristics, reflecting different compositions of mantle sources and parental magmas, degree of partial melting, fractional crystallization and assimilation of crustal materials. The primary high-Ti magmas were derived from an enriched and deep mantle source, and may have undergone fractional crystallization of clinopyroxene+plagioclase without crustal contamination. The LREE-depleted picrites were derived from a strongly depleted mantle source and formed by high degrees of anhydrous melting at relatively shallow mantle depths, whereas the LREE-enriched picrite indicates a mantle source locally modified by subducted oceanic crust. The low-Ti basalts formed from picritic melts by AFC processes. Extensive crustal contamination may have resulted in S-oversaturation and sulfide segregation in some of the low-Ti basaltic magmas. Those low-Ti basalts with relatively high PGE contents and positive $\varepsilon Nd(t)$ values formed from weakly contaminated magmas and did not experience significant sulfide segregation. Those formed from highly contaminated magmas have low PGE contents and very negative $\varepsilon Nd(t)$ values and experienced substantial sulfide segregation.

Acknowledgments

This study was substantially supported by a research grant from the Research Grants Council of Hong Kong, China (HKU7057/05P) and an outstanding researcher award from Chinese Academy of Sciences (2005-2-21). Dr. Danping Yan from Chinese University of Geosciences and Drs. Chi Cung Thuong and Hoang Huu Thanh from the Institute of Geological Sciences, Vietnam, are thanked for their field assistance in northern Vietnam. We also thank Ms. Xiao Fu for help with sample analyses and Dr. Junhong Zhao for helpful discussions. On the authors' request, Profs. Paul T. Robinson, Ian H. Campbell and Catherine Chauvel and Dr. Rebbeca Sproule provided comments on an early draft of this paper. Official reviews by Dr. Peter C. Lightfoot and Prof. Sun-Lin Chung and editorial handling by Prof. S. Goldstein are gratefully acknowledged.

Appendix A. Measured major oxide compositions (wt.%) of the standards used for XRF analyses

Standards	BHVO-2 (basalt)			GSP-2 (granodiorite)			BCR-2 (basalt)		
	This study	Expected	Accuracy (%)	This study	Expected	Accuracy (%)	This study	Expected	Accuracy (%)
SiO_2	49.99	49.90	−0.18	66.75	66.60	−0.23	54.52	54.10	−0.77
TiO_2	2.73	2.73	−0.17	0.67	0.66	−1.46	2.29	2.26	−1.25
Al_2O_3	13.56	13.50	−0.45	14.86	14.90	0.28	13.51	13.50	−0.08
Fe_2O_3T	12.35	12.30	−0.43	4.94	4.90	−0.79	13.88	13.80	−0.55
MnO	0.17			0.04			0.20	0.20	−3.45
MgO	7.45	7.23	−3.06	0.96	0.96	−0.38	3.66	3.59	−1.91
CaO	11.58	11.40	−1.56	2.13	2.10	−1.53	7.28	7.12	−2.21
Na_2O	2.27	2.22	−2.21	2.65	2.78	4.57	3.10	3.16	1.99
K_2O	0.52	0.52	0.38	5.46	5.38	−1.49	1.80	1.79	−0.77
P_2O_5	0.27	0.27	−1.14	0.30	0.29	−2.77	0.37	0.35	−4.57
LOI	−0.40	−0.40	0.00	0.65	0.65	0.00	0.12	0.12	0.00
Total	101.17			99.82			101.09		

Appendix B. Measured trace element compositions (ppm) of the standards used for ICP-MS analyses

	BHVO-1 (basalt)			AMH-1 (andesite)			GBPG-1(garnet–biotite-plagiogneiss)			OU-6 (slate)		
	Expected (1)	This work	Accuracy (%)	Expected (2)	This study	Accuracy (%)	Expected (3)	This study	Accuracy (%)	Expected (4)	This study	Accuracy (%)
Sc	31.8	28.1	11.7	13.5	14.9	−10.5	13.9	15.1	−8.6	22.1	22.1	−0.1
V	317	321.7	−1.5	106	112	−5.3	96.5	96.7	−0.2	129	119	7.6
Cr	289	289.6	−0.2	40.9	42.0	−2.8	181	172	5.0	70.8	67.4	4.7
Co	45	46.3	−2.9	18.7	19.2	−2.8	19.5	19.4	0.3	29.1	28.3	2.9
Ni	121	119	2.0	32.4	33.0	−2.0	59.6	49.9	16.3	39.8	40.5	−1.7
Cu	136	134	1.2	30.2	32.5	−7.7	30.0	31.9	−6.2	39.6	41.1	−3.8
Zn	105	106	−0.6	66.9	71.3	−6.6	80.3	79.3	1.3	111	111	0.1
Rb	11	9.66	12.2	18.3	18.4	−0.5	56.2	56.7	−0.9	120	117	2.7
Sr	403	394	2.2	545	559	−2.5	364	369	−1.6	131	134	−2.6
Ba	139	125	10.0	322	327	−1.3	908	905	0.4	477	480	−0.6
Y	27.6	26.6	3.6	16.4	15.2	7.4	18.0	18.6	−3.2	27.4	26.6	2.9
Zr	179	170	5.1	146	149	−2.3	232	239	−3.1	174	178	−2.3
Hf	4.38	4.35	0.6	3.70	3.86	−4.3	6.07	6.37	−5.0	4.70	5.05	−7.4
Nb	19	18.3	3.7	8.32	7.97	4.2	9.93	9.90	0.3	14.8	14.2	3.7
Ta	1.23	1.25	−1.7	0.64	0.64	−0.5	0.40	0.43	−7.2	1.06	1.05	1.3
Cs	0.13	0.12	6.9	0.24	0.25	−5.9	0.32	0.35	−8.4	8.02	8.30	−3.5
Pb	2.6	2.15	17.5	9.85	9.27	5.9	14.1	13.3	6.0	28.2	29.7	−5.2
Th	1.08	1.19	−10.4	2.64	2.70	−2.2	11.2	12.3	−9.2	11.5	12.0	−4.2
U	0.42	0.42	1.0	0.89	0.89	0.4	0.90	0.95	−5.9	1.96	2.01	−2.4
La	15.8	15.0	5.1	15.9	16.9	−6.2	53.0	52.5	0.8	33.0	34.1	−3.2
Ce	39	36.9	5.3	33.0	35.1	−6.4	103	102	0.9	74.4	78.4	−5.4
Pr	5.7	5.24	8.1	4.21	4.51	−7.1	11.5	12.0	−4.5	7.80	8.36	−7.1
Nd	25.2	23.7	5.8	17.7	18.1	−2.3	43.3	42.7	1.5	29.0	31.1	−7.1
Sm	6.2	5.91	4.7	3.68	3.86	−5.0	6.79	6.68	1.7	5.92	6.22	−5.1
Eu	2.06	2.12	−2.9	1.16	1.19	−2.6	1.79	1.81	−1.1	1.36	1.42	−4.7
Gd	6.4	6.02	5.9	3.34	3.23	3.3	4.74	5.23	−10.4	5.27	5.42	−2.8
Tb	0.96	0.94	2.5	0.51	0.53	−3.4	0.60	0.64	−6.9	0.85	0.86	−1.3
Dy	5.2	5.15	0.9	2.84	2.93	−3.3	3.26	3.34	−2.5	4.99	5.11	−2.3
Ho	0.99	0.97	2.0	0.57	0.59	−4.4	0.69	0.72	−3.6	1.01	1.06	−4.7
Er	2.4	2.47	−2.8	1.52	1.55	−1.9	2.01	2.19	−9.1	2.98	3.01	−1.2
Tm	0.33	0.32	1.7	0.21	0.22	−3.6	0.30	0.31	−2.7	0.44	0.43	3.2
Yb	2.02	1.98	2.2	1.37	1.41	−3.1	2.03	2.21	−8.9	3.00	3.02	−0.6
Lu	0.291	0.28	3.2	0.21	0.21	−1.2	0.31	0.34	−10.5	0.45	0.44	2.4

Note: expected values for standards: (1) from Govindaraju (1994); (2) from Thompson et al. (2000); (3) from Potts et al. (2000); (4) from Potts and Kane (2005).

Appendix C. GPS locations of samples

Sample no.	GPS location	Sample no.	GPS location
HK-01	20°48.85′N, 105°19.88′E	HK-73	21°16.33′N, 104°14.90′E
HK-02	20°48.89′N, 105°19.64′E	HK-74	21°16.33′N, 104°14.90′E
HK-04	20°48.89′N, 105°19.64′E	HK-76	21°16.49′N, 104°14.81′E
HK-05	20°48.89′N, 105°19.64′E	HK-77	21°16.49′N, 104°14.81′E
HK-06	20°48.89′N, 105°19.64′E	HK-80	21°14.87′N, 104°13.77′E
HK-11	20°45.60′N,105°20.03′E	HK-81	21°14.87′N, 104°13.77′E
HK-13	20°45.60′N, 105°20.03′E	HK-84	21°14.87′N, 104°13.77′E
HK-14	20°45.60′N, 105°20.03′E	HK-85	21°13.43′N, 104°11.14′E
HK-17	21°40.11′N, 103°37.97′E	HK-86	21°13.43′N, 104°11.14′E
HK-22	21°40.32′N, 103°37.46′E	HK-87	21°13.43′N, 104°11.14′E
HK-24	21°40.32′N, 103°37.46′E	HK-89	21°13.43′N, 104°11.14′E
HK-30	21°39.94′N, 103°37.68′E	HK-90	21°13.16′N, 104°11.03′E
HK-35	21°31.14′N, 103°43.35′E	HK-92	21°13.26′N, 104°10.81′E
HK-36	21°31.14′N, 103°43.35′E	HK-93	21°13.66′N, 104°10.04′E
HK-37	21°31.14′N, 103°43.35′E	HK-94	21°11.13′N, 104°12.26′E
HK-38	21°31.14′N, 103°43.35′E	HK-95	21°11.13′N, 104°12.26′E
HK-39	21°31.14′N, 103°43.35′E	HK-96	21°11.13′N, 104°12.26′E
HK-40	21°29.24′N, 103°46.97′E	HK-97	21°11.10′N, 104°12.62′E
HK-41	21°29.24′N, 103°46.97′E	HK-98	21°11.10′N, 104°12.62′E
HK-42	21°29.32′N, 103°46.72′E	HK-99	21°10.86′N, 104°12.98′E
HK-43	21°29.32′N, 103°46.72′E	JP-3	22°41.35′N, 103°08.85′E
HK-44	21°29.32′N, 103°46.72′E	JP-4	22°41.41′N, 103°08.84′E
HK-46	21°29.79′N, 103°46.31′E	JP-5	22°41.41′N, 103°08.84′E
HK-47	21°30.30′N, 103°45.27′E	JP-6	22°41.43′N, 103°08.87′E
HK-48	21°30.30′N, 103°45.27′E	JP-7	22°41.88′N, 103°09.25′E
HK-49	21°30.34′N, 103°45.19′E	JP-8	22°42.15′N, 103°09.73′E
HK-50	21°30.34′N, 103°45.19′E	JP-9	22°42.25′N, 103°09.62′E
HK-51	21°30.34′N, 103°45.19′E	JP-10	22°42.35′N, 103°09.53′E
HK-52	21°31.26′N, 103°43.27′E	JP-11	22°42.70′N, 103°09.77′E
HK-53	21°31.26′N, 103°43.27′E	JP-12	22°42.70′N, 103°09.77′E
HK-59	21°30.89′N, 103°43.53′E	JP-13	22°42.70′N, 103°09.77′E
HK-60	21°22.78′N, 103°46.74′E	JP-14	22°42.70′N, 103°09.77′E
HK-61	21°22.61′N, 103°46.83′E	JP-16	22°43.25′N, 103°10.09′E
HK-62	21°22.61′N, 103°46.83′E	JP-19	22°42.68′N, 103°10.80′E
HK-63	21°20.44′N, 103°52.52′E	JP-21-1	22°42.88′N, 103°10.99′E
HK-64	21°20.02′N, 103°52.91′E	JP-21-2	22°42.88′N, 103°10.99′E
HK-65	21°20.02′N, 103°52.91′E	JP-22	22°42.88′N, 103°10.99′E
HK-67	21°16.33′N, 104°14.90′E	JP-25	22°47.19′N, 103°12.17′E
HK-69	21°16.33′N, 104°14.90′E	JP-26	22°47.19′N, 103°12.17′E
HK-70	21°16.33′N, 104°14.90′E	JP-27	22°47.12′N, 103°12.32′E
HK-71	21°16.33′N, 104°14.90′E	JP-28	22°47.12′N, 103°12.32′E
HK-72	21°16.33′N, 104°14.90′E		

References

Aldanmaz, E., Pearce, J.A., Thirlwall, M.F., Mitchell, J.G., 2000. Petrogenetic evolution of late Cenozoic, post-collision volcanism in western Anatolia, Turkey. J. Volcanol. Geotherm. Res. 102, 67–95.

Anders, E., Grevesse, N., 1989. Abundances of the elements: meteoritic and solar. Geochim. Cosmochim. Acta 53, 197–214.

Andersen, J.C.O., Power, M.R., Momme, P., 2002. Platinum-group elements in the Paleogene North Atlantic igneous province. In: Cabri, L.J. (Ed.), The Geology, Geochemistry, Mineralogy and Mineral Beneficiation of Platinum-Group Elements. Ottawa Ontario. Can. Inst. Min. Met. Spec., vol. 54, pp. 637–667.

Arndt, N.T., Christensen, U., 1992. Role of lithospheric mantle in continental volcanism: thermal and geochemical constraints. J Geophys. Res. 97, 10967–10981.

Arndt, N.T., Chauvel, C., Czamanske, G., Fedorenko, V., 1998. Two mantle sources, two plumbing systems: tholeiitic and alkaline magmatism of the Maynecha River basin, Siberian flood volcanic province. Contrib. Mineral. Petrol. 133, 297–313.

Barnes, S.-J., Maier, W.D., 1999. The fractionation of Ni, Cu and the noble metals in silicate and sulfide liquids. In: Keays, R.R., Lesher, C.M., Lightfoot, P.C., Farrow, C.E.G. (Eds.), Dynamic Processes in Magmatic Ore Deposits and Their Application to Mineral Exploration. Geol. Assoc. Can, Short Course Notes, vol. 13, pp. 69–106.

Barnes, S.-J., Picard, C.P., 1993. The behavior of platinum-group elements during partial melting, crystal fractionation and sulphide segregation: an example from the Cape Smith fold belt, northern Quebec. Geochim. Cosmochim. Acta 57, 79–87.

Barnes, S.-J., Naldrett, A.J., Gorton, M.P., 1985. The origin of the fractionation of platinum-group elements in terrestrial magmas. Chem. Geol. 53, 303–323.

Brügmann, G.E., Naldrett, A.J., Asif, M., Lightfoot, P.C., Gorbachev, N.S., Fedorenko, V.A., 1993. Siderophile and chalcophile metals as tracers of the evolution of the Siberian trap in the Noril'sk region, Russia. Geochim. Cosmochim. Acta 57, 2001–2018.

Campbell, I.H., 1998. The mantle chemical structure: insights from the melting products of mantle plumes. In: Jackson, I. (Ed.), The Earth's Mantle: Composition, Structure, and Evolution. Cambridge University Press, New York, pp. 259–310.

Campbell, I.H., Griffiths, R.W., 1990. Implications of mantle plume structure for the evolution of flood basalts. Earth Planet. Sci. Lett. 99, 79–93.

Carlson, R.W., 1991. Physical and chemical evidence on the cause and source characteristics of flood basalt volcanism. Aust. J. Earth Sci. 38, 525–544.

Chen, J.F., Jahn, B.M., 1998. Crustal evolution of southeastern China: Nd and Sr isotopic evidence. Tectonophysics 284, 101–133.

Chen, F.K., Siebel, W., Satir, M., Terzioğlu, M.N., Saka, K., 2002. Geochronology of the Karadere basement (NW Turkey) and implications for the geological evolution of the Istanbul zone. Int. J. Earth Sci. 91, 469–481.

Chen, F.K., Li, X.H., Wang, X.L., Li, Q.L., Siebel, W., in press. Zircon age and Nd–Hf isotopic composition of the Yunnan Tethyan belt, southwestern China. Int. J. Earth Sci. doi:10.1007/s00531-006-0146-y.

Chung, S.L., Jahn, B.M., 1995. Plume–lithosphere interaction in generation of the Emeishan flood basalts at the Permian–Triassic boundary. Geology 23, 889–892.

Chung, S.L., Lee, T.L., Lo, C.H., Wang, P.L., Chen, C.Y., Yem, N.T., Hoa, T.T., Wu, G.Y., 1997. Intraplate extension prior to continental extrusion along the Ailao Shan–Red River shear zone. Geology 25, 311–314.

Depaolo, D.J., 1988. Neodymium Isotope Geochemistry: An Introduction. Springer Verlag, New York.

Ely, J.C., Neal, C.R., 2003. Using platinum-group elements to investigate the origin of the Ontong Java Plateau, SW Pacific. Chem. Geol. 196, 235–257.

Ernst, R.E., Buchan, K.L., Campbell, I.H., 2005. Frontiers in large igneous province research. Lithos 79, 271–297.

Gao, S., Lin, W.L., Qiu, Y.M., 1999. Contrasting geochemical and Sm–Nd isotopic compositions of Archaean metasediments from the Kongling high-grade terrain of the Yangtze craton: evidence for cratonic evolution and redistribution of REE during crustal anatexis. Geochim. Cosmochim. Acta 63, 2071–2088.

Glotov, A.I., Polyakov, G.V., Hoa, T.T., Balykin, P.A., Akimtsev, V.A., Krivenko, A.P., Tolstykh, N.D., Phuong, N.T., Thanh, H.H., Hung, T.Q., Petrova, T.E., 2001. The Ban Phuc Ni–Cu–PGE deposit related to the Phanerozoic komatiite–basalt association in the Song Da rift, northwestern Vietnam. Can. Mineral. 39, 573–589.

Govindaraju, K., 1994. Compilation of Working Values and Sample Description for 383 Geostandards. Geostand. News, vol. 18. (Spe. Issu.), 158 pp.

Green, T.H., 1994. Experimental studies of trace-element partitioning applicable to igneous petrogenesis — Sedona 16 years later. Chem. Geol. 117, 1–36.

Griselin, M., Arndt, N.T., 1996. Plume–lithosphere interaction and crustal contamination during formation of Coppermine River basalts, Northwest Territories, Canada. Can. J. Earth Sci. 34, 958–975.

Guo, F., Fan, W.M., Wang, Y., Li, C., 2004. When did the Emeishan mantle plume activity start? Geochronological and geochemical evidence from ultramafic–mafic dikes in Southwestern China. Int. Geol. Rev. 46, 226–234.

Hanski, E., Walker, R.J., Huhma, H., Polyakov, G.V., Balykin, P.A., Hoa, T.T., Phuong, N.T., 2004. Origin of the Permian–Triassic komatiites, northwestern Vietnam. Contrib. Mineral. Petrol. 147, 453–469.

Hergt, J.M., Chappell, B.W., McCulloch, M.T., McDougall, I., Chivas, A.R., 1989. Geochemical and isotopic constraints on the origin of the Jurassic dolerites of Tasmania. J. Petrol. 30, 841–883.

Herzberg, C., Zhang, J.Z., 1996. Melting experiments on anhydrous peridotite KLB-1: compositions of magmas in the upper mantle and transition zone. J. Geophys. Res. 101, 8271–8295.

Jenner, G.A., Longerich, H.P., Jackson, S.E., Fryer, B.J., 1990. ICP-MS—a powerful tool for high precision trace element analyses in earth sciences: evidence from analyses of selected USGS reference samples. Chem. Geol. 83, 133–148.

Keays, R.R., 1995. The role of komatiitic and picritic magmatism and S-saturation in the formation of the ore deposits. Lithos 34, 1–18.

Keays, R.R., Lightfoot, P.C., 2007. Siderophile and chalcophile metal variations in Tertiary picrites and basalts from West Greenland with implications for the sulphide saturation history of continental flood basalt magmas. Miner. Depos. 42, 319–336.

Kerr, A., 2003. Nickeliferous gabbroic intrusions of the Pants Lake area, Labrador, Canada: implications for the development of magmatic sulfides in mafic systems. Am. J. Sci. 303, 221–258.

Kieffer, B., Arndt, N.T., Lapierre, H., Bastien, F., Bosch, D., Pecher, A., Yirgu, G., Ayalew, D., Weis, D., Jerram, D.A., Keller, F., Meugniot, C., 2004. Flood and shield basalts from Ethiopia: magmas from the African superswell. J. Petrol. 45, 793–834.

Lacassin, R., Leloup, P.H., Trinh, P.T., Tapponnier, P., 1998. Unconformity of red sandstones in north Vietnam: field evidence for Indosinian orogeny in northern Indochina? Terra Nova 10, 106–111.

Larsen, L.M., Pedersen, A.K., Sundvoll, B., Frei, R., 2003. Alkali picrites formed by melting of old metasomatized lithospheric mantle: Manîtdlat Member, Vaigat Formation, Paleocene of West Greenland. J. Petrol. 44, 3–38.

Lightfoot, P.C., Hawkesworth, C.J., 1997. Flood basalts and magmatic Ni, Cu, and PGE sulfide mineralization: comparative geochemistry of the Noril'sk (Siberian trap) and West Greenland sequences. Geophys. Monogr. 100, 357–380.

Lightfoot, P.C., Keays, R.R., 2005. Siderophile and chalcophile metal variations in flood basalts from the Siberian Trap, Noril'sk Region: implications for the origin of the Ni–Cu–PGE sulfide ores. Econ. Geol. 100, 439–462.

Lightfoot, P.C., Sutcliffe, R.H., Doherty, W., 1991. Crustal contamination identified in Keweenawan Osler Group tholeiites, Ontario: a trace element perspective. J. Geol. 99, 739–750.

Lightfoot, P.C., Hawkesworth, C.J., Hergt, J., Naldrett, A.J., Gorbachev, N.S., Fedorenko, V.A., Doherty, W., 1993. Remobilization of the continental lithosphere by mantle plumes: major-, trace-element and Sr-, Nd-, and Pb-isotope evidence from picritic and tholeiitic lavas of the Noril'sk district, Siberian Trap, Russia. Contrib. Mineral. Petrol. 114, 171–188.

Lightfoot, P.C., Naldrett, A.J., Gorbachev, N.S., Fedorenko, V.A., Hawkesworth, C.J., Doherty, W., 1994. Chemostratigraphy of the Siberian Trap Lava, Noril'sk district, Russia. Implications for sources of flood basalt magma and their associated Ni–Cu mineralization. Ont. Geol. Surv. Spec. Publ. 5, 283–312.

Ma, C.Q., Ehlers, C., Xu, C.H., 2000. The roots of the Dabieshan ultrahigh-pressure metamorphic terrain: constraints from geochemistry and Nd–Sr isotope systematics. Precambrian Res. 102, 279–301.

MacDonald, G.A., Katsura, T., 1964. Chemical composition of Hawaiian lavas. J. Petrol. 5, 82–133.

Meisel, T., Moser, J., 2004. Reference materials for geochemical PGE analysis: new analytical data for Ru, Rh, Pd, Os, Ir, Pt and Re by isotope dilution ICP-MS in 11 geological reference materials. Chem. Geol. 208, 319–338.

Naldrett, A.J., 2004. Magmatic Sulfide Deposits: Geology, Geochemistry and Exploration. Springer, Germany.

Peach, C.L., Mathez, E.A., Keays, R.R., Reeves, S.J., 1994. Experimental determination of sulfide melt–silicate melt partition coefficients for iridium and palladium. Chem. Geol. 117, 361–377.

Pirajno, F., 2000. Ore Deposits and Mantle Plumes. Kluwer Acad., Dordrecht, Neth, p. 556.

Polyakov, G.V., Balykin, P.A., Glotov, A.I., Tran, Q.H., Ngo, T.P., Hoang, H.T., Bui, A.N., 1991. Permian–Triassic association of high-magnesian volcanic rocks of the Song Da zone (northwestern Vietnam). Sov. Geol. Geophys. 32, 1–11 (in Russian).

Polyakov, G.V., Balykin, P.A., Tran, T.H., Ngo, T.P., Hoang, H.T., Tran, Q.H., Ponomarchuk, V.A., Lebedev, Y., Kireev, A.D., 1998. Evolution of the Mesozoic–Cenozoic magmatism in the Song Da rift and its contouring structures (northwestern Vietnam). Sov. Geol. Geophys. 39, 695–706 (in Russian).

Potts, P.J., Kane, J.S., 2005. International association of geoanalysts certificate of analysis: certified reference material OU-6 (Penrhyn slate). Geostand. Geoanaly. Res. 29, 233–236.

Potts, P.J., Thompson, M., Kane, J.S., Petrov, L.L., 2000. GeoPT 7 — An International Proficiency Test for Analytical Geochemistry Laboratory-Report on Round 7/(Garnet–Biotite Plagiogneiss).

Qi, L., Hu, J., Gregoire, D.C., 2000. Determination of trace elements in granites by inductively coupled plasma-mass spectrometry. Talanta 51, 507–513.

Qi, L., Zhou, M.-F., Wang, C.Y., 2004. Determination of low concentrations of platinum group elements in geological samples by ID-ICP-MS. J. Anal. At. Spectrom. 19, 1335–1339.

Qi, L., Zhou, M.-F., Wang, C.Y., Sun, M., in press. Evaluation of the determination of Re and PGEs abundance of geological samples by ICP-MS coupled with a modified Carius tube digestion at different temperatures. Geochem. J.

Saunders, A.D., Fitton, J.G., Kerr, A.C., Norry, M.J., Kent, R.W., 1997. The North Atlantic Igneous Province. In: Mahoney, J.J., Coffin, M.F. (Eds.), Large Igneous Provinces: Continental, Oceanic and Planetary Flood Volcanism. Am. Geophys. Union, Washington DC, pp. 45–93.

Song, X.Y., Zhou, M.-F., Hou, Z.Q., Cao, Z.M., Wang, Y., Li, Y., 2001. Geochemical constraints on the mantle source of the Upper Permian Emeishan continental flood basalts, southwestern China. Int. Geol. Rev. 43, 213–225.

Song, X.Y., Zhou, M.-F., Keays, R.R., Cao, Z.M., Sun, M., Qi, L., 2006. Geochemistry of the Emeishan flood basalts at Yangliuping, Sichuan, SW China: implications for sulfide segregation. Contrib. Mineral. Petrol. 152, 53–74.

Späth, A., Le Roex, A.P., Opiyo-Akech, N., 2001. Plume–lithosphere interaction and the origin of continental rift-related alkaline volcanism—the Chyulu Hills volcanic province, southern Kenya. J. Petrol. 42, 765–787.

Staudigel, H., Hart, S.R., 1983. Alteration of basaltic glass: mechanisms and significance for the oceanic crust–seawater budget. Geochim. Cosmochim. Acta 47, 337–350.

Sun, S.S., McDonough, W.F., 1989. Chemical and isotopic systematics of oceanic basalts: implications for mantle composition and processes. In: Saunders, A.D., Norry, M.J. (Eds.), Magmatism in the Ocean Basins. Geol. Soc. Spec. Publ., vol. 42, pp. 313–345.

Thompson, R.N., Gibson, S.A., 2000. Transient high temperatures in mantle plume heads inferred from magnesian olivines in Phanerozoic picrites. Nature 407, 502–506.

Thompson, M., Potts, P.J., Kane, J.S., Wilson, S., 2000. GeoPT5. An international proficiency test for analytical geochemistry laboratories — report on round 5 (August 1999). Geostand. Geoanaly. Res. 24, E1–E28.

Wang, C.Y., Zhou, M.-F., 2006. Genesis of the Permian Baimazhai magmatic Ni–Cu–(PGE) sulfide deposit, Yunnan, SW China. Miner. Depos. 41, 771–783.

Wang, X.F., Metcalfe, I., Jian, P., He, L.Q., Wang, C.S., 2000. The Jinshajiang–Ailaoshan Suture Zone, China: tectonostratigraphy, age and evolution. J. Asian Earth Sci. 18, 675–690.

Wang, C.Y., Zhou, M.-F., Keays, R.R., 2006. Geochemical constraints on the origin of the Permian Baimazhai mafic–ultramafic intrusion, SW China. Contrib. Mineral. Petrol. 152, 309–321.

White, R.S., McKenzie, D., 1995. Mantle plumes and flood basalts. J. Geophys. Res. 100, 17543–17585.

Wilson, M., 1989. Igneous Petrogenesis. Unwin Hyman, London, pp. 245–285.

Wooden, J.L., Czamanske, G.K., Fedorenko, V.A., Arndt, N.T., Chauvel, C., Bouse, R.M., King, B.W., Knight, R.J., Siems, D.F., 1993. Isotopic and trace-element constraints on mantle and crustal contributions to Siberian continental flood basalts, Noril'sk area, Siberia. Geochim. Cosmochim. Acta 57, 3677–3704.

Wu, G.Y., 1993. Permian basalts in Lijiang and Jinping, western Yunnan: a comparative study and its geologic significance:. Acta Petrol. Sin. 9, 63–69 (supple., in Chinese with English abstract).

Wyllie, P.J., 1981. Plate tectonics and magma genesis. Geol. Rundsch. 70, 128–153.

Xiao, L., Xu, Y.G., Chung, S.L., He, B., Mei, H.J., 2003. Chemostratigraphic correlation of Upper Permian lavas from Yunnan Province, China: extent of the Emeishan large igneous province. Int. Geol. Rev. 45, 753–766.

Xiao, L., Xu, Y.G., Mei, H.J., Zheng, Y.F., He, B., Pirajno, F., 2004. Distinct mantle sources of low-Ti and high-Ti basalts from the western Emeishan large igneous province, SW China: implications for plume–lithosphere interaction. Earth Planet. Sci. Lett. 228, 525–546.

Xu, Y.G., Chung, S.L., Jahn, B.M., Wu, G.Y., 2001. Petrologic and geochemical constraints on the petrogenesis of Permian–Triassic Emeishan flood basalts in southwestern China. Lithos 58, 145–168.

Xu, Y.G., He, B., Chung, S.-L., Menzies, M.A., Frey, F.A., 2004. Geologic, geochemical, and geophysical consequences of plume involvement in the Emeishan flood-basalt province. Geology 32, 917–920.

YBGMR (Yunnan Bureau of Geology and Mineral Resources), 2000. Regional Geology of Yunnan Province. Geol Publ Press, Beijing. (in Chinese).

Zhang, H.F., Sun, M., Lu, F.X., Zhou, X.M., Zhou, M.-F., Liu, Y.S., Zhang, G.H., 2001. Moderately depleted lithospheric mantle underneath the Yangtze Block: evidence from a garnet lherzolite xenolith in the Dahongshan kimberlite. Geochem. J. 35, 315–331.

Zhou, M.-F., Malpas, J., Song, X.Y., Kennedy, A.K., Robinson, P.T., Sun, M., Lesher, C.M., Keays, R.R., 2002. A temporal link between the Emeishan large igneous province (SW China) and the end-Guadalupian mass extinction. Earth Planet. Sci. Lett. 196, 113–122.

Zhou, M.-F., Robinson, P.T., Lesher, C.M., Keays, R.R., Zhang, C.J., Malpas, J., 2005. Geochemistry, petrogenesis, and metallogenesis of the Panzhihua gabbroic layered intrusion and associated Fe–Ti–V-oxide deposits, Sichuan Province, SW China. J. Petrol. 46, 2253–2280.

Zhou, M.-F., Zhao, J.H., Qi, L., Su, W.C., Hu, R.Z., 2006. Zircon U–Pb geochronology and elemental and Sr–Nd isotope geochemistry of Permian mafic rocks in the Funing area, SW China. Contrib. Mineral. Petrol. 151, 1–19.

Zindler, A., Hart, S.R., 1986. Chemical geodynamics. Annu. Rev. Earth Planet. Sci. 14, 493–571.